Christian-Albrechts-Universität zu Kiel
Chair of Information and Coding Theory
Prof. Dr.-Ing. Peter Adam Höher

Short Range Localization Algorithms for an Underwater Swarm

Master Thesis in Electrical and Information Engineering

by
Maureen Petersilka

First Referee: Prof. Dr.-Ing. Peter Adam Höher
Second Referee: Dr.-Ing. Siwei Zhang

Oberpfaffenhofen, October 31, 2025

Declaration

I declare that I have produced the Master's thesis "Short Range Localization Algorithms for an Underwater Swarm" independently and without improper external assistance and that I have identified all word-for-word quotations of other authors, as well as comments based closely on other authors' ideas, and I have listed the relevant sources.

I am aware that, unless agreed otherwise, the Master's thesis produced under supervision represents a group achievement and forms part of the overall research of the supervising institution. As a result, none of the co-authors (e.g. authors of text, creative project staff, co-supervisors) may use passages from the thesis for commercial purposes or make them accessible to third parties without the (written) approval of all those involved due to reasons of copyright. Particular note must be taken of the Arbeitnehmererfindergesetz (German Employee Invention Act), according to which pre-publication of patent-related content is prohibited.

Oberpfaffenhofen, October 31, 2025

M. Petersilka

Maureen Petersilka

Acknowledgements

I would like to express deepest gratitude to my supervisor Prof. Dr.-Ing. Peter Adam Höher from the chair of information and coding theory at Christian-Albrechts-Universität zu Kiel for providing me the opportunity to carry out his research and for his valuable academic supervision.
My sincere thanks also go out to my supervisor at DLR, Dr. Siwei Zhang, for his continuous support, valuable guidance and constructive feedback throughout the course of this thesis.
Finally I am sincerely grateful to the team at DLR for their collaboration and support during this time. Special thanks go to Dr. Ing. Michael Walter and Dr.-Ing. Armin Dammann who have contributed immensely to my work by providing valuable insights and guidance through the course of my thesis.

Abstract

To this day there is no universal localization system for underwater environments. To address this limitation, swarm-based localization approaches are gaining attention since they enable the estimation of the relative position between multiple vehicles. In those systems, multiple Autonomous Surface Vehicles and Autonomous Underwater Vehicles create a local reference frame, enabling coordinated navigation without the need for an external localization system.

Due to the complexity and inherent limitations of the underwater environment, this localization is generally based on acoustic ranging between the vehicles.

The thesis presents the potential and limitations of short range acoustic localization, with particular focus on environmental variability, sensor geometry and estimation accuracy. It is demonstrated that both the Particle Filter and the Extended Kalman Filter, when combined with suitable initialization, facilitate accurate and continuous position estimations, provided that geometric constraints and maximum range limitations are taken into account.

These findings are substantiated by data collected during a dedicated measurement campaign, validating the theoretical analysis and highlighting the practical challenges of real-world deployment.

Zusammenfassung

Da bis heute kein universelles Lokalisierungssystem für Unterwasserumgebungen existiert, gelten schwarmbasierte Lokalisierungsverfahren als vielversprechender Ansatz für die Unterwasserlokalisierung, weil diese die Schätzung der relativen Position zwischen den einzelnen Einheiten ermöglichen. In diesen Systemen erstellen mehrere autonome Oberflächen- und Unterwasser- fahrzeuge einen lokalen Referenzrahmen, der eine koordinierte Navigation ohne ein externes Lokalisierungssystem ermöglicht. Aufgrund der Komplexität und den inherenten Einschränkungen der Unterwasserumgebung basiert diese Lokalisierung generell auf akustischen Entfernungsmessungen zwischen den Fahrzeugen.

Die Masterarbeit veranschaulicht das Potential und die Grenzen der akustischen Nahbereichslokalisierung unter Berücksichtigung von Umweltvariabilitäten, Sensorgeometrie und Schätzgenauigkeit. Es wird dargestellt, dass sowohl der Particle Filter als auch der Extended Kalman Filter in Kombination mit einer geeigneten Initialisierung genaue und kontinuierliche Positionsschätzung ermöglichen, sofern geometrische Einschränkungen sowie maximale Entfernungsbegrenzungen berücksichtigt werden.

Diese Ergebnisse werden durch in der Ostsee aufgenommene Messdaten bekräftigt, wodurch die theoretische Analyse bestätigt und die praktischen Herausvorderungen in der realen Welt hervorgehoben werden.

Contents

Acronyms

ASV	Autonomous Surface Vehicle
AUV	Autonomous Underwater Vehicle
AWGN	Additive White Gaussian Noise
BCRLB	Biased Cramér Rao lower bound
CRLB	Cramér Rao Lower Bound
DLR	German Aerospace Center
EKF	Extended Kalman Filter
EM	Electromagnetic
FIM	Fisher Information Matrix
GNSS	Global Navigation Satellite Systems
GPS	Global Positioning System
IWLS	Iterative Weighted Least Suqares
LoS	Line of Sight
MAP	Maximum A-Posteriori
ML	Maximum Likelihood
MSE	Mean Square Error
NLoS	Non Line of Sight
PCRLB	Posterior Cramér Rao lower bound
PDF	Probability Density Function
PF	Particle Filter
PL	Propagation Loss
PSD	Power Spectral Density
RMSE	Root Mean Square Error
RTToF	Round Trip Time of Flight
RWILS	Regularized Weighted Iterative Least Squares
SNR	Signal-to-Noise Ratio
SOFAR	Sound Fixing and Ranging

SSP	Sound Speed Profile
ToF	Time of Flight

1. Introduction

1.1. Motivation

In recent years, awareness of the critical importance of knowledge about the underwater environment has grown significantly. Incidents such as the break down of Nord Stream 1 and 2 [1], the loss of the Titan submersible during its mission to the Titanic wreck [2], and ongoing geopolitical developments have emphasized the increasing relevance of reliable situational awareness below the ocean surface [3].
Achieving such awareness requires advanced sensing technologies as well as precise knowledge of where these measurements originate. Accurate localization therefore is fundamental for any underwater observation, inspection, or communication system. Establishing reliable underwater positioning thus forms a major step toward improving situational awareness and enabling coordinated autonomous operations.
While Global Navigation Satellite Systems (GNSS), such as the Global Positioning System (GPS) and Galileo [4] allow for precise terrestrial localization and navigation, underwater localization remains a significant challenge. This is due to the fact that in underwater environments, Electromagnetic (EM) waves such as radio signals and visible light are strongly attenuated due to high absorption and scattering in seawater. Therefore, acoustic signals, which are only slightly attenuated underwater, are the primary means for underwater communication and localization [5]. However, other challenges arise since the underwater channel is highly variable, influenced by changes in temperature, salinity and pressure. These properties cause sound speed variations, resulting in effects like refraction, multipath propagation, and signal distortion. Therefore, underwater localization systems must adapt to these dynamic environmental conditions [6].
The development of the proposed localization framework is based on a swarm system comprised of multiple Autonomous Surface Vehicles (ASV) and Autonomous Underwater Vehicles (AUV). Since ASVs and AUVs typically operate in clusters, only short range communication and localization is required. This thesis therefore

focuses on short range transmission scenarios, which serve as a foundation for future swarm-based localization system. The influence of the channel characteristics, such as spatial variations in the sound speed and the resulting refraction of acoustic rays, on the propagation paths and corresponding Time of Flight (ToF) measurements is investigated. The analysis further addresses how these effects contribute to localization bias. Based on these findings, a simplified swarm localization system is developed, which aims to track the trajectory of an AUV based on Round Trip Time of Flight (RTToF) measurements between the AUV and multiple ASVs. The developed localization scheme is then tested on experimental data, obtained by a measurement campaign conducted by the German Aerospace Center (DLR), to determine the feasibility of the underlying system.

1.2. Outline

In order to address the challenges of underwater swarm localization and the development of suitable estimation algorithms, this thesis is divided into eight chapters. The motivation, objective, and an the general structure of the thesis is introduced in Chapter 1. In Chapter 2, an overview of the underwater acoustic channel and its fundamental properties, including attenuation, ambient noise, and sound propagation is provided. Moreover, a channel simulator is introduced, and the characteristics of ASVs and AUVs are discussed. The chapter concludes with a summary of the theoretical fundamentals of estimation theory. The measurement setup and data generation process, which account for real-world conditions in the context of the localization simulations, are described in Chapter 3. The various localization algorithms investigated in this work are presented in Chapter 4. The initial estimations involve static algorithms that localize the AUV based on snapshot information. Subsequently, two recursive filters are presented, which extend the estimations to track a continuous trajectory of the AUV. Within Chapter 5 the simulation results are discussed and the performance of the implemented localization algorithms, based on the principles introduced in the preceding chapters, is presented. The application of the developed algorithms to experimental data is outlined in Chapter 6. The key findings of this thesis are summarized in Chapter 7, and potential improvements together with future research directions related to underwater swarm localization are presented in Chapter 8.

2. Fundamentals

This chapter provides the background information required for this thesis. This includes details of the characteristics of the underwater channel, a simulator for the propagation of acoustic waves, ASVs and AUVs as well as the fundamentals of estimation theory.

2.1. Underwater Channel

The underwater channel is a model of highly complex propagation environment that exhibits unique characteristics concerning signal transmission. Its varying properties, particularly with regard to attenuation, require a careful selection of the transmission signal.

2.1.1. Propagation Loss

An important aspect to consider when examining a communication channel is the Propagation Loss (PL) experienced by different types of signals, which depends primarily on the traveled distance and the attenuation of the transmitted signal.
Electromagnetic (EM) waves, for instance, are well suited for communication in air due to their high data rates and low propagation delay. In the underwater environment, however, especially high-frequency EM waves are severely attenuated, particularly in seawater. This attenuation of EM waves is dependent on the properties of the medium, mainly magnetic and dielectric permittivity, as well as the electrical conductivity. While the magnetic permeability underwater is approximately equal to that in air, the dielectric permittivity and the electrical conductivity of seawater are significantly higher due to the presence of dissolved ions (salt) and polar molecules. As a result, EM waves experience exponential decay with increasing distance, leading to an effective range of a few meters, thus rendering them unsuitable for underwater localization [5].

In contrast, acoustic waves present a practical alternative for underwater communication due to their relatively low attenuation in seawater. Their total PL is modeled as the product of their geometric spreading and frequency dependent absorption

$$A(d, f) = d^k \alpha(f)^d \tag{2.1}$$

[7]. Here, k denotes the spreading factor, which characterizes the geometry of the signal propagation. It's value ranges from 1 to 2, with $k = 1$ corresponding to cylindrical spreading and $k = 2$ to spherical spreading. For high-frequency signals, the absorption coefficient in dB can be calculated with

$$10 \log \alpha(f) = 0.11 \times \frac{f^2}{1 + f^2} + 44 \times \frac{f^2}{4100 + f^2} + 2.75 \times 10^{-4} f^2 + 0.003, \tag{2.2}$$

where f is the frequency denoted in kilohertz (e.g. $f = 10\,\text{kHz}$ corresponds to $f = 10$). The absorption coefficient for acoustic and EM signals as a function of frequency is illustrated in Figure 2.1.

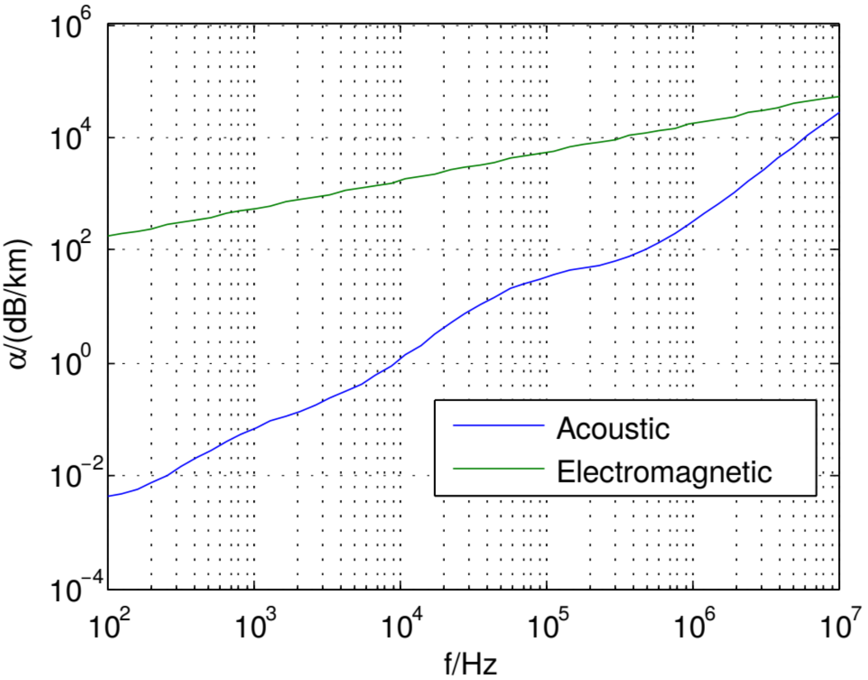

Figure 2.1.: The attenuation of EM and acoustic waves underwater as a function of frequency [8].

It is evident that, particularly for lower frequencies, the attenuation of acoustic signals remains considerably lower in comparison to EM signals, rendering them more suitable for underwater communication. Consequently, the measurement system considered in this thesis is based on acoustic signals.

2.1.2. Noise

Another important aspect in signal transmission is the noise associated with the respective system, as it directly influences the Signal-to-Noise Ratio (SNR) of the measurements. In underwater environments, ambient and site-specific noise must be considered [9]. Ambient noise is present throughout the ocean, caused by factors such as currents, shipping or rain, and is often approximated as Additive White Gaussian Noise (AWGN). The Power Spectral Density (PSD) of the ambient noise is frequency dependent and can be determined with

$$10 \log N(f) = 10 \log \left(N_{\mathrm{t}}(f) + N_{\mathrm{s}}(f) + N_{\mathrm{w}}(f) + N_{\mathrm{th}}(f)\right), \tag{2.3}$$

where $N_{\mathrm{t}}(f)$, $N_{\mathrm{s}}(f)$, $N_{\mathrm{w}}(f)$ and $N_{\mathrm{th}}(f)$ denote the noise components due to turbulence, ships, wind and thermal effects, respectively and can be calculated with

$$10 \log N_{\mathrm{t}}(f) = 17 - 30 \log (f), \tag{2.4}$$

$$10 \log N_{\mathrm{s}}(f) = 40 + 20(\mathrm{s} - 0.5) + 26 \log (f) - 60 \log (f + 0.03), \tag{2.5}$$

$$10 \log N_{\mathrm{w}}(f) = 50 + 7.5\mathrm{w}^{\frac{1}{2}} + 20 \log (f) - 40 \log (f + 0.4), \tag{2.6}$$

$$10 \log N_{\mathrm{th}}(f) = -15 + 20 \log (f) \tag{2.7}$$

[7]. While noise caused by turbulence only influences very low frequencies ($f \leq 10\,\mathrm{Hz}$), shipping activities dominate the noise in the frequency region of $10\,\mathrm{Hz} \leq f \leq 100\,\mathrm{Hz}$. Wind leads to surface motion, which is the major factor contributing to the noise for frequencies $100\,\mathrm{Hz} \leq f \leq 100\,\mathrm{kHz}$ and thermal noise is dominant for frequencies above 100 kHz [9]. The PSD of the noise for varying levels of shipping activity and wind speed for the frequencies up to 100 kHz is illustrated in Figure 2.2, which shows that the noise PSD primarily decreases with frequency.

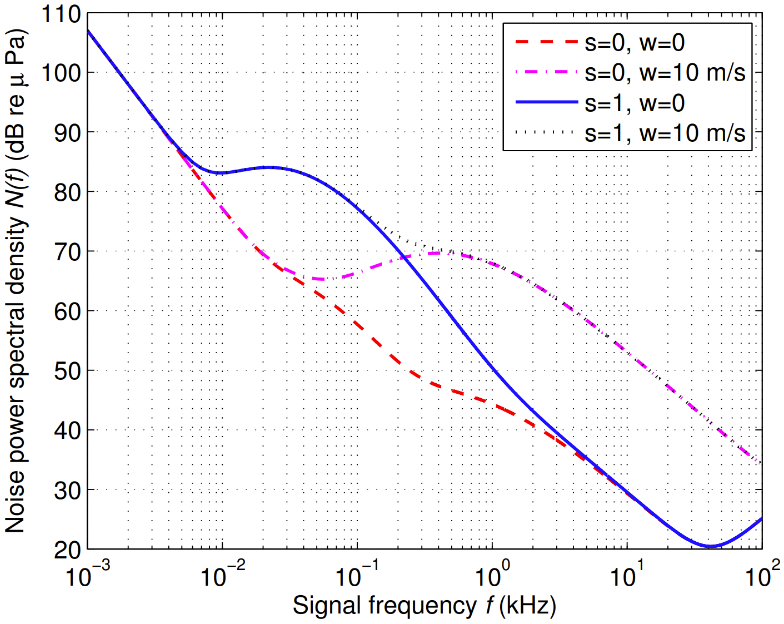

Figure 2.2.: Ambient noise underwater as a function of frequency [7][1].

In contrast, site-specific noise is only perceptible in particular places, for example near wind farms, due to ice cracking in polar regions or as a result of other localized sources. Unlike ambient noise, it generally contains non-Gaussian components [10]. Since this thesis focuses on general underwater communication scenarios, only ambient noise will be considered.

2.1.3. Sound Speed Profile

In underwater environments, the speed of sound is not constant but depends primarily on pressure, temperature, and salinity, with values ranging between 1450 and 1540 m/s [11]. Within a given water mass, these properties mainly change with depth; therefore the sound speed is commonly expressed as a function of depth ($c(z)$). The resulting curve is referred to as the Sound Speed Profile (SSP) [11]. However, salinity and temperature are not only depth-dependent, but also vary with location and, especially in shallow regions, can change considerably over time due to seasonal effects or long-term trends such as global warming.

An example of this effect can be observed in the Baltic Thalweg, for which the local temperature distribution is shown in Figures 2.3(a) and 2.3(b) for February

---

[1] s = 0 denotes low shipping activity and s = 1 high shipping activity.

and August 2019, respectively. A substantial seasonal variation is apparent, with shallow-water temperatures increasing from approximately 3 °C to 5 °C in February to about 17 °C to 19 °C in August. Consequently, an SSP is often only valid for the specific time and place from which it is derived.

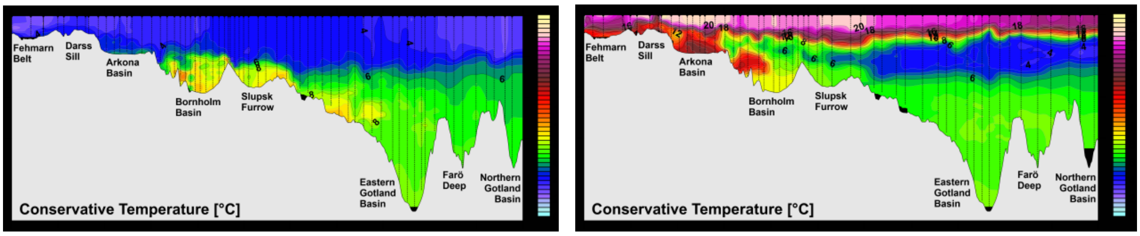

(a) February (b) August

Figure 2.3.: Temperature profiles along the Baltic Thalweg for February (a) and August (b) 2019 [12].

A variety of mostly statistical models for the SSP exists, differing in complexity and intended application purposes. In shallow regions, the sound speed generally decreases monotonically with depth, primarily caused by the downward-decreasing temperature profile. This decline in sound velocity is illustrated in Figure 2.4(a), which shows the SSP of a coastal region in the Gotland Basin for August 2019 (latitude: 54.5927849, longitude: 11.0795898). It is computed based on the Medwin model (2.8) with depth dependent data about the temperature and salinity collected by the Leibniz Institut für Ostseeforschung Warnemünde in August 2019 [12]. This profile serves as the foundation for subsequent simulations in coastal regions that rely on a depth-dependent SSP. The Medwin model is an empirical formula, widely used for shallow marine environments. It is valid for temperatures of $0\,°\mathrm{C} \leq T \leq 35\,°\mathrm{C}$, salinities of $0\,‰ \leq S \leq 45\,‰$ and depths z up to 1000 m

$$c = 1449.2 + 4.6T - 0.055T^2 + 0.00029T^3 + (1.34 - 0.010T)(S - 35) + 0.016z \quad (2.8)$$

[11].

In deep-sea regions, the sound speed typically decreases near the surface due to cooling, reaches a minimum at a depth of approximately 1200 m - depending on the ocean - and then increases again due to pressure. This characteristic shape is represented by the Munk profile, shown in Figure 2.4(b), which is a classic analytical model describing the sound speed in deep-sea regions:

$$c(z) = c_0[1 + \epsilon(\mathrm{e}^{-\eta} - (1 - \eta))], \tag{2.9}$$

where η denotes the depth of the minimum sound speed and ϵ the magnitude of the deviation from this minimum [13].

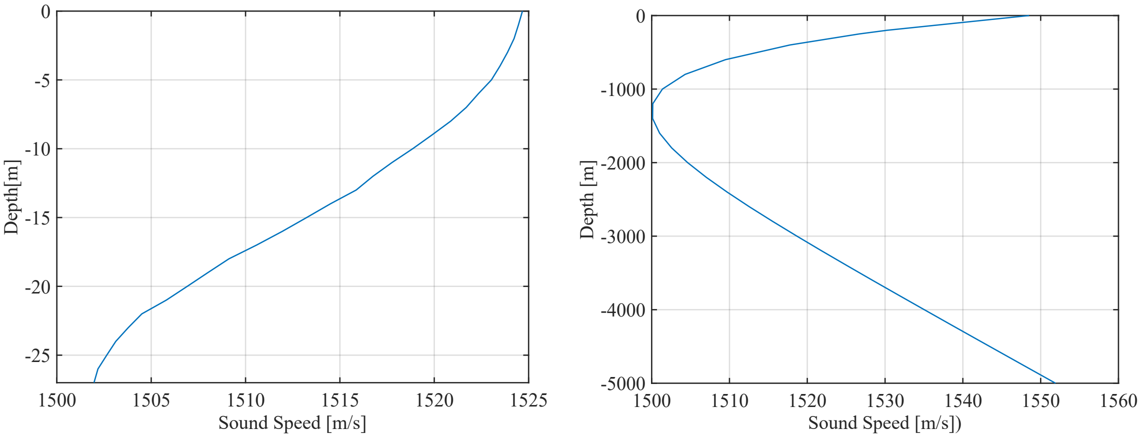

(a) Coastal region in the Gotland Basin (b) Deep-sea region (Munk profile)

Figure 2.4.: SSP for (a) a coastal region in Gotland Basin and (b) for a deep-sea regions (Munk profile).

2.1.4. Sound Propagation

The SSP leads to a nonlinear propagation of acoustic waves, as variations in the sound speed cause changes in the refractive properties of the water. This effect is described by Snell's Law, which displays the relationship between the angles of incidence and refraction of waves passing through a boundary layer between two media [11].

In the domain of underwater acoustics, acoustic waves are frequently modelled as rays, an approach particularly prevalent in ray-tracing simulations. In such models, each ray represents a discrete propagation path of energy. The curvature of these rays is determined by the local sound speed gradient with the rays bending towards regions of lower sound speed. In the ocean, where the sound speed changes continuously with depth, the refraction of sound rays is described by

$$\frac{\cos\beta(z)}{c(z)} = \text{const.} \tag{2.10}$$

[14]. Since in shallow water, the sound speed $c(z)$ is often approximated as monotonically decreasing with depth, the sound rays are predominantly bent downward, leading to a propagation profile dominated by reflections at the bottom and surface of the ocean. This behaviour is illustrated in Figure 2.5(a), which depicts the modeled ray paths for a coastal region with a sender depth of 5 m. The different colours indicate the number of reflections: red corresponds to a rays without reflections, green to rays with one reflection at the surface, blue to rays with one reflection at the bottom and black rays undergo multiple reflections.

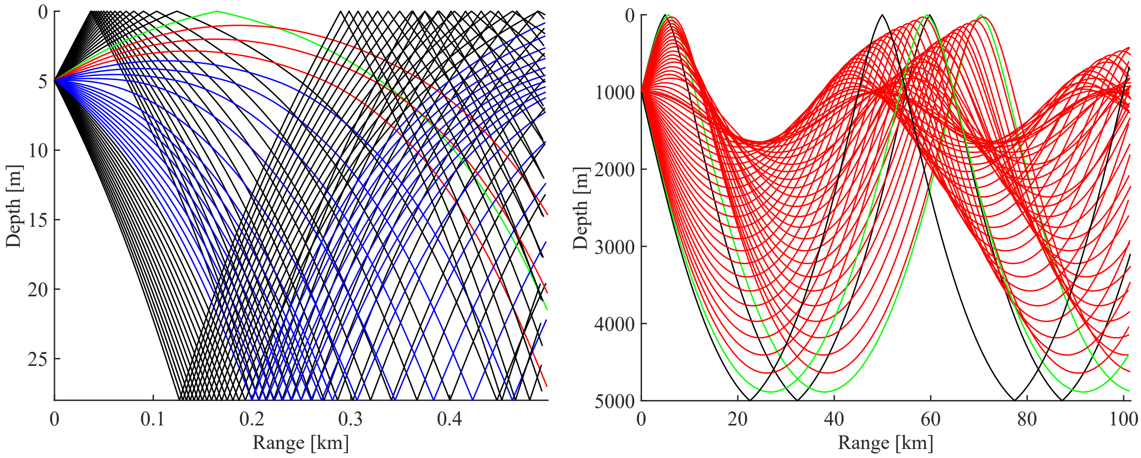

(a) Coastal region in the Gotland Basin

(b) SOFAR channel

Figure 2.5.: Propagation of sound rays in (a) a coastal region in the Gotland Basin and in (b) the SOFAR channel.

In contrast, for deep-sea regions, the sound speed profile often exhibits a minimum at a certain depth, forming the Sound Fixing and Ranging (SOFAR) channel. Rays above this minimum experience downward refraction, while rays below it are refracted upward, creating a waveguide effect and thus enabling sound rays to propagate over distances of several thousand kilometers. This phenomenon is illustrated in Figure 2.5(b), which displays the ray paths in a deep-sea environment with the same color scheme as in Figure 2.5(a).

The curvature of the sound rays can result in regions, where no direct Line of Sight (LoS) connection exists between the transmitter and receiver. Furthermore, the combination of multiple ray launch angles and boundary reflections results in mulipath propagation, causing different rays with distinct travel times and intensities to arrive between the same source-receiver pair. This complicates the analysis of the received signals, since it can be difficult to distinguish between the different arrivals.

2.2. Bellhop Simulator

Bellhop is a widely used acoustic ray-tracing program designed for modeling sound propagation in depth dependent ocean environments [15]. It simulates the effects of refraction due to variations in the SSP as well as reflections at the sea surface and bottom. By launching a fan of rays at different take-off angles from the source, Bellhop computes both general ray trajectories and eigenrays that directly connect a source-receiver pair. This enables the extraction of key propagation characteristics such as travel times, angles of arrival and the occurrence of multipath propagation. In addition to eigenray analysis, Bellhop can calculate propagation-loss fields, visualize acoustic ray paths, and estimate the distribution of received signal intensity. All simulation parameters - including acoustic frequency, source and receiver geometry, the SSP, bottom properties, and the file output type - are specified in a dedicated environmental file, which ensures reproducibility and flexible scenario design.

2.3. Autonomous Surface and Underwater Vehicles

Autonomous Surface Vehicle (ASV) are unmanned robotic vehicles, that are located on the sea surface and are primarily used for environmental monitoring or marine research. They operate based on various, mostly electrical or hybrid, propulsion systems [16]. For the purpose of the DLR measurements, the ASVs are equipped with GNSS sensors, hydrophones to record and transmit acoustic signals, as well as onboard processing units for signal analysis.

Autonomous Underwater Vehicle (AUV) are similarly unmanned robotic systems that operate below the sea surface and usually navigate along pre-programmed routes. AUVs are commonly deployed for tasks such as seabed mapping or environmental monitoring. In the DLR setup, the AUVs are likewise equipped with hydrophones and processing units, enabling acoustic communication with the ASVs.

2.4. Estimation Theory

Estimation theory is a branch of statistics that deals with determining numerical values for unknown parameters based on sample data, which is obtained via measurements or simulations. There are different aspects to consider when evaluating the performance of an estimator.

2.4.1. Unbiased and Biased Estimation

Let Θ denote the true parameter and $\hat{\Theta}$ an estimation computed from available data. An estimator is considered unbiased, if the expectation of the estimation is the parameter itself

$$E\{\hat{\Theta}\} = \Theta. \tag{2.11}$$

Otherwise the estimator exhibits a nonzero systematic error which is called bias

$$E\{\hat{\Theta}\} = \Theta + \text{bias}. \tag{2.12}$$

Here, the systematic error refers to the deterministic offset of the mean from the true value, whereas the random error is quantified by the estimator's variance [17].

2.4.2. Cramér Rao Lower Bound

To evaluate the performance of an estimator the Mean Square Error (MSE) or Root Mean Square Error (RMSE) of the estimation is often analyzed. Within this thesis, the so called Cramér Rao Lower Bound (CRLB) is used to determine the theoretical minimal achievable error for the considered estimator. The CRLB is derived under the regularity condition and based on the Cauchy-Schwarz inequality. Since a complete derivation would exceed the scope of this thesis, only a shortened version is presented here. A more detailed derivation can be found in [17].

For an unbiased estimator, the CRLB directly bounds the variance of the estimated parameter $\hat{\Theta}$ and for biased estimators, a generalized form exists in which both the variance and the bias contribute to the lower bound. In both cases the CRLB defines the theoretical limit of achievable estimation accuracy, based on the expectation of the estimator $E\{\hat{\Theta}\}$ and the Probability Density Function (PDF) $p(y|\Theta)$ of the observed measurements, given the unknown parameter:

$$\mathrm{VAR}\{\hat{\Theta}(y)\} \geq \frac{|\frac{\mathrm{d}}{\mathrm{d}\Theta} E\{\hat{\Theta}\}|^2}{E\{|\frac{\mathrm{d}}{\mathrm{d}\Theta} \ln p(y|\Theta)|^2\}}. \tag{2.13}$$

Cramér Rao Lower Bound for Scalar Parameters

For an unbiased estimator, the expected value of the estimation equals the true parameter. Under this condition, (2.13) simplifies to

$$\mathrm{VAR}\{\hat{\Theta}(y)\} \geq \frac{1}{E\left\{\left|\frac{\mathrm{d}}{\mathrm{d}\Theta}\ln p(y|\Theta)\right|^2\right\}}. \tag{2.14}$$

For individual measurements y_i the observation consists of a signal component s_i, dependent on the parameter Θ and an noise term

$$y_i = s_i(\Theta) + n_i, \qquad i = 1, ..., m, \tag{2.15}$$

where m denotes the number of measurements. If n_i is zero-mean and statistically independent AWGN with variance σ^2, the PDF of the measurement values is given by

$$p(y|\Theta) = \frac{1}{\sqrt{2\pi\sigma^2}}\mathrm{e}^{-\frac{(s_i(\Theta)-y_i)^2}{2\sigma^2}}, \tag{2.16}$$

which leads to the following variance bound for the estimation of the parameter Θ based on the observations y_i:

$$\mathrm{VAR}\{\hat{\Theta}\} \geq \frac{\sigma^2}{\sum_{i=1}^{m}\left(\frac{\mathrm{d}}{\mathrm{d}\Theta}s_i(\Theta)\right)^2}. \tag{2.17}$$

For ToF estimations, where the signals are observed sample by sample, the measurements can be expressed as

$$y_i = s(iT - \tau) + n_i, \tag{2.18}$$

with T representing the sampling time and τ the time delay, which leads to the following threshold for the variance in the time domain:

$$\mathrm{VAR}\{\hat{\Theta}\} \geq \frac{\sigma^2}{2\sum_{i=1}^{m}\left(\frac{\mathrm{d}}{\mathrm{d}\tau}s_i(iT-\tau)\right)^2}. \tag{2.19}$$

The factor σ^2 in the denominator shows that the CRLB depends linearly on the variance of the noise, and consequently the SNR.
Examining the properties of the CRLB in the frequency domain, reveals that it is

dependent on the characteristics of the signal as well. For a sampled, bandlimited signal with the sampling time $T = \frac{1}{B}$, the signal can be expressed as

$$s(iT) = \int_{-\frac{1}{2T}}^{+\frac{1}{2T}} S(f)\mathrm{e}^{\mathrm{j}2\pi fiT}\,\mathrm{d}f, \tag{2.20}$$

with $S(f)$ denoting the spectrum of the signal in the Fourier domain. A derivation of the CRLB using the property $\mathcal{F}\{\frac{\mathrm{d}}{\mathrm{d}t}x(t)\} = \mathrm{j}2\pi f X(f)$ as well as Parseval's theorem leads to

$$\mathrm{VAR}\{\hat{\Theta}\} \geq \frac{\sigma^2 T}{8\pi^2 \int_{-\frac{1}{2T}}^{+\frac{1}{2T}} f^2|S(f)|^2\,\mathrm{d}f} \tag{2.21}$$

(derivation in [17]). As the signal energy is distributed more widely in the higher frequencies, the integral over $f^2|S(f)|$ increases and consequently the lower bound decreases.

When assuming a signal with unlimited Bandwidth $B = \frac{1}{T} \rightarrow \infty$ with the noise PSD $N_0 = \sigma^2 T = \frac{\sigma^2}{B}$, the variance threshold can be expressed as

$$\mathrm{VAR}\{\hat{\tau}\} \geq \frac{1}{8\pi^2 \frac{E_s}{N_0}\beta^2}, \tag{2.22}$$

which reveals that the lower variance threshold of the timing estimation is inversely proportional to the SNR. The effective bandwidth β can be calculated with

$$\beta = \sqrt{\frac{\int_{-\infty}^{+\infty} f^2|S(f)|^2\,\mathrm{d}f}{\int_{-\infty}^{+\infty} |S(f)|^2\,\mathrm{d}f}}. \tag{2.23}$$

Cramér Rao Lower Bound for Vector Parameters

The information an observation contains about one of the parameters is denoted within the so called Fisher Information. When considering a parameter vector with multiple estimation parameters $\mathbf{\Theta} = [\Theta_1, \Theta_2, ..., \Theta_n]$, the Fisher information is a matrix, with the size (No. parameters × No. observations). For the unbiased case, the **CRLB** matrix is the inverse of the Fisher Information Matrix (**FIM**)

$$\mathbf{CRLB} = \mathbf{FIM}^{-1} \tag{2.24}$$

[17]. In case of an AWGN channel, the **FIM** can be calculated with the Jacobian matrix $\mathbf{J}$ and the covariance matrix $\mathbf{\Sigma}$

$$\mathbf{FIM} = \mathbf{J}^T \mathbf{\Sigma}^{-1} \mathbf{J}. \tag{2.25}$$

The Jacobian Matrix $\mathbf{J}$, contains the partial derivatives of the individual measurement functions $(h_1, ..., h_m)$ with respect to the different parameters $(\Theta_1, ...\Theta_n)$

$$\mathbf{J} = \begin{bmatrix} \frac{\partial h_1}{\partial \Theta_1} & \frac{\partial h_1}{\partial \Theta_2} & \cdots & \frac{\partial h_1}{\partial \Theta_n} \\ \frac{\partial h_2}{\partial \Theta_1} & \frac{\partial h_2}{\partial \Theta_2} & \cdots & \frac{\partial h_2}{\partial \Theta_n} \\ \vdots & \vdots & \ddots & \vdots \\ \frac{\partial h_m}{\partial \Theta_1} & \frac{\partial h_m}{\partial \Theta_2} & \cdots & \frac{\partial h_m}{\partial \Theta_n} \end{bmatrix}. \tag{2.26}$$

The covariance matrix $\mathbf{\Sigma}$ consists of the variances and covariances of the various measurements

$$\mathbf{\Sigma} = \begin{bmatrix} \sigma_{1,1}^2 & \sigma_{1,2} & \cdots & \sigma_{1,m} \\ \sigma_{2,1} & \sigma_{2,2}^2 & \cdots & \sigma_{2,m} \\ \vdots & \vdots & \ddots & \vdots \\ \sigma_{m,1} & \sigma_{m,2} & \cdots & \sigma_{m,m}^2 \end{bmatrix}. \tag{2.27}$$

Posterior Cramér Rao Lower Bound

For iterative estimation methods (e.g., recursive filters), where information from the previous estimation step is carried forward, the CRLB must be extended accordingly. In such cases, the Posterior Cramér Rao lower bound (PCRLB) is calculated. It is based on the PDF of the estimates, the measurement and transition model, as well as the a-priori information about the parameters. Its computation is performed iteratively as

$$\mathbf{J}_{n+1} = \mathbf{D}_n^{22} - \mathbf{D}_n^{21}(\mathbf{J}_n + \mathbf{D}_n^{11})^{-1}\mathbf{D}_n^{12} \tag{2.28}$$

[18]. Here, $\mathbf{J}_n$ denotes the Fisher Information at the time step n, such that the posterior variance bound corresponds to inverse of $\mathbf{J}_n$. The submatrices $\mathbf{D}_n^{11}$, $\mathbf{D}_n^{12}$, $\mathbf{D}_n^{21}$ and $\mathbf{D}_n^{22}$ are defined based on the expected values of the measurement and the transition model. For an AWGN channel the submatrices can be calculated with

$$\mathbf{D}_n^{11} = E\{[\nabla_{x_n} f_n^T(x_n)]\mathbf{Q}_n^{-1}[\nabla_{x_n} f_n^T(x_n)]^T\}, \tag{2.29}$$

$$\mathbf{D}_n^{12} = -E\{[\nabla_{x_n} f_n^T(x_n)]\mathbf{Q}_n^{-1}\}, \tag{2.30}$$

$$\mathbf{D}_n^{21} = [\mathbf{D}_n^{21}]^T, \tag{2.31}$$

$$\mathbf{D}_n^{22} = \mathbf{Q}_n^{-1} + E\{[\nabla_{x_{n+1}} h_{n+1}^T(x_{n+1})]\mathbf{R}_{n+1}^{-1}[\nabla_{x_{n+1}} h_{n+1}^T(x_{n+1})]^T\}, \tag{2.32}$$

with $\mathbf{Q}_n$ and $\mathbf{R}_n$ denoting the covariance matrices of the transition and measurement noise, respectively [18]. The transition model is defined as

$$\mathbf{x}_{n+1} = f_n(\mathbf{x}_n) + \mathbf{w}_n = \mathbf{F}_n\mathbf{x}_n + \mathbf{w}_n \tag{2.33}$$

and the measurement model as

$$\mathbf{z}_n = h_n(\mathbf{x}_n) + \mathbf{v}_n = \mathbf{H}_n\mathbf{x}_n + \mathbf{v}_n. \tag{2.34}$$

For a linear transition model, the deviation of the transition model is constant thus the expectation of the deviation can be neglected ($\nabla x_n f_n^T(x_n) = \mathbf{F}_n$). Therefore, the calculations of the submatrices $\mathbf{D}_n^{11}$ and $\mathbf{D}_n^{12}$ simplify to

$$\mathbf{D}_n^{11} = \mathbf{F}_n^T\mathbf{Q}_n^{-1}\mathbf{F}_n, \tag{2.35}$$

$$\mathbf{D}_n^{12} = -\mathbf{F}_n^T\mathbf{Q}_n^{-1}. \tag{2.36}$$

In case of a single estimation incorporating a-priori knowledge, a shortened version of the PCRLB applies, in which prior information is directly added to the Fisher Information

$$\mathbf{FIM} = \mathbf{FIM}_{\text{meas}} + \mathbf{FIM}_{\text{prior}} \tag{2.37}$$

Cramér Rao Lower Bound for Biased Estimators

When dealing with biased estimators, the CRLB also has to account for the error introduced by the bias. In this case, the numerator of the variance bound includes the deviation of the expected value of the estimator

$$\text{VAR}\{\hat{\Theta}(y)\} \geq \frac{|\frac{\mathbf{d}}{\mathbf{d}\Theta}E\{\hat{\Theta}\}|^2}{E\{|\frac{\mathbf{d}}{\mathbf{d}\Theta}\ln p(y|\Theta)|^2\}}. \tag{2.38}$$

The total estimation error is therefore represented by including the bias term in this bound. This way, the CRLB for biased estimation (BCRLB) provides a lower bound on the MSE instead of only on the variance of the estimates. Thus, for a given parameter i, the BCRLB can be expressed as

$$E\{\Theta - \hat{\Theta}\} \geq \mathbf{b}_i^2(\Theta) + \{[\mathbf{I} + \nabla_\Theta(\mathbf{b})]\mathbf{FIM}^{-1}[\mathbf{I} + \nabla_\Theta(\mathbf{b})]^T\}_{ii}, \tag{2.39}$$

where $\mathbf{b}$ denotes a vector containing bias functions of each parameter Θ_i, the index i indicates the corresponding Parameter, $\mathbf{I}$ is the identity matrix, and **FIM** denotes the Fisher Information Matrix [19].

3. Measurement System and Data Simulation

This chapter describes the measurement system and the simulation framework used to generate synthetic data for the localization of the AUV. The experimental setup, consisting of four ASVs and one AUV as illustrated in Figure 3.1, is designed to reflect realistic conditions in coastal environments, including the depth dependent SSP.

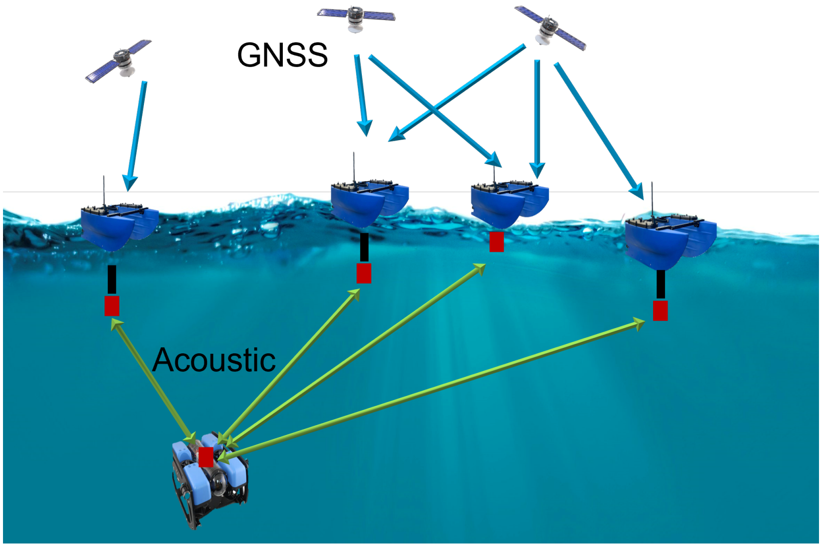

Figure 3.1.: Measurement setup employed for the simulations.

The positions of the vehicles are represented in three dimensions by vectors containing their coordinates along the x-, y-, and z-axes in meter

$$\mathbf{r}_\mathrm{a} = [x_\mathrm{a}, y_\mathrm{a}, z_\mathrm{a}]^T \mathrm{m}, \tag{3.1}$$

$$\mathbf{r}_i = [x_i, y_i, z_i]^T \mathrm{m}, \quad i \in \{1, ..., 4\}. \tag{3.2}$$

The index a denotes the AUV and the index i represents the ASVs, which remain fixed throughout the simulations. The ASVs are equipped with GNSS receivers mounted above the water surface, which allow accurate position determination; therefore, their positions are assumed to be known. Communication between the ASVs and the AUV is established via acoustic signals with a carrier frequency of 40 kHz. Since the Bellhop simulator does not support the simulation of signal waveforms (e.g., chirp, OFDM, pulse), the specific signal waveform is not explicitly modeled in this thesis. However, the system is assumed to operate with signals characterized by a well-defined effective bandwidth β and initial energy E_0. The hydrophones of the ASVs, employed for transmission and reception, are mounted at a depth of 30 cm beneath the surface of the sea.

For the purposes of the simulation scenarios, an area of interest is defined, for which the ASV geometry is optimized to achieve accurate localization. The area in question is a square area of $2500\,\mathrm{m}^2$, located in a horizontal plane parallel to the sea surface at a depth of 10 m. Furthermore, while the current simulations assume fixed ASVs, future designs could support extensions in which the ASVs are mobile and capable of following the AUV. Such a setup would enable extended trajectories beyond the limitations of fixed anchor configurations.

The coordinate system is defined such that the origin $[0, 0, 0]^{\mathrm{T}}\mathrm{m}$ coincides with the point on the water surface directly above the center of the square of the area of interest. The x- and y- axes lie in the horizontal plane, while the z-axis is oriented vertically, with negative values corresponding to increasing depth. Consequently, the ASVs are positioned at $z = -0.3\,\mathrm{m}$, while the AUV operates at $z = -10\,\mathrm{m}$.

3.1. Joint Ranging and Sound Speed Estimation

The underwater environment is unknown and spatially varying, particularly in coastal regions. Therefore, accurate localization of the AUV requires joint estimation of its 3D position and the average sound speed along the acoustic propagation path. This necessity arises from the fact that the sound speed directly affects the Round Trip Time of Flight (RTToF) measurements used for ranging, and any error in its assumed value propagates into localization inaccuracies. The parameter vector is thus defined as $\boldsymbol{\Theta} = [x_{\mathrm{a}}, y_{\mathrm{a}}, z_{\mathrm{a}}, c]^{\mathrm{T}}$, where $x_{\mathrm{a}}, y_{\mathrm{a}}$ and z_{a} denote the AUVs position coordinates, and c the average sound speed.

To obtain the RTToF measurements, acoustic signals are transmitted from the individual ASVs to the AUV, where they are processed, amplified, and retransmitted back to the respective ASVs. The measured propagation delay τ_i provides information about the distance d_i between the ASV_i and the AUV as well as the average sound speed c. This relationship can be expressed by the measurement function $h(\boldsymbol{\Theta})$, which depends on the parameter vector $\boldsymbol{\Theta}$ and shows an idealized relation between the parameters and the time delay

$$\tau_{\text{ideal}} = h(\boldsymbol{\Theta}) = \frac{2d_i}{c}, \tag{3.3}$$

with

$$d_i = \sqrt{(x_{\text{a}} - x_i)^2 + (y_{\text{a}} - y_i)^2 + (z_{\text{a}} - z_i)^2}. \tag{3.4}$$

The corresponding measurement model accounts for random deviations in the measured time delays and can therefore be expressed as

$$\tau_i = h(\Theta) + \epsilon, \tag{3.5}$$

where ϵ represents zero-mean Gaussian measurement noise with a variance that depends on the distance between the ASV and the AUV (Section 3.3.1).

Since both the 3D position of the AUV and the average sound speed c are unknown, the set of equations derived from four RTToF measurements results in a system with four unknowns. Solving this can be achieved by using the measurements obtained from the four different ASVs.

As stated beforehand, due to the SSP, the propagation paths of the sound waves are not linear, but bent on a curve. For rays in this scenario, where the ASVs hydrophones are 30 cm underneath the surface and the AUVs at 10 m depth, this behaviour is illustrated in Figure 3.2. The color coding of the rays is analogous to that used for Figures 2.5(a) and 2.5(b).

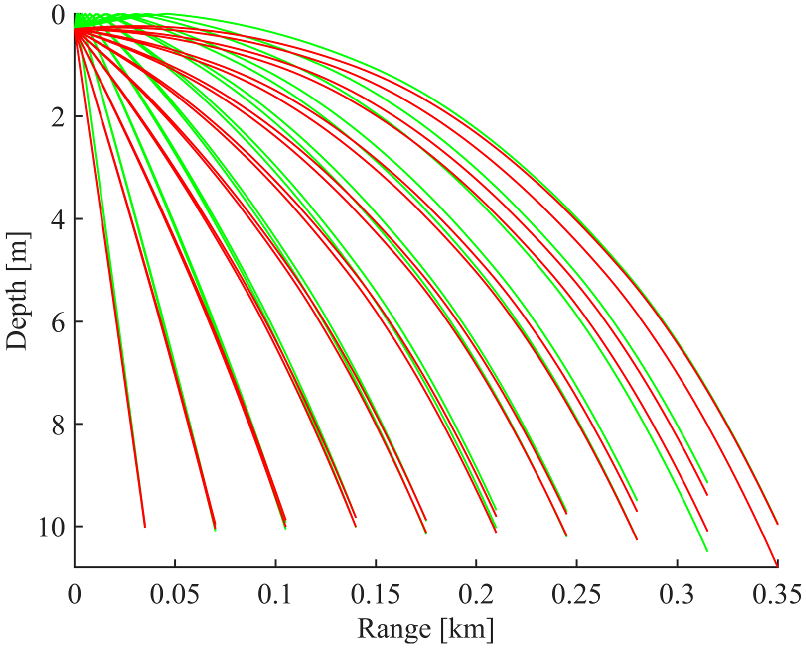

Figure 3.2.: Propagation profile for a sender depth of 0.3 m and a receiver depth of 10 m.

For the calculation of distances during the ranging process, an Euclidean distance between the transmitter and the receiver is assumed. This leads to a modelling error, dependent on the curvature of the rays. In Table 3.1 the difference between the Euclidean distance and the travelled distance for various horizontal ranges with a transmitter depth of 0.3 m and a receiver depth of 10 m are shown.

horizontal range [m]	travelled dist. [m]	euclidean dist. [m]	deviation [%]
10	14.705	14.705	6.9e-05
20	24.234	24.234	2.76 e-04
50	56.382	56.381	1.67e-03
100	100.449	100.444	4.96e-03

Table 3.1.: Difference between the travelled and Euclidean distances for different horizontal ranges.

It can be observed, that the differences between the Euclidean distances and the travelled paths are insignificant and can therefore be neglected for short range applications.

Another impact of the depth dependent SSP and the resulting ray curvature is the occurrence of an effective average sound speed along the propagation path. With the available measurements it is only possible to estimate an average sound speed and not the whole, depth dependent SSP. However, an approximation of a constant average sound speed for all four propagation paths during the given time period introduces a model inaccuracy. This inaccuracy arises because the average sound speed experienced by each acoustic ray depends on its specific propagation path, which in turn is determined by the vertical gradient of the SSP. For instance, in the coastal region in the Gotland Basin the sound speed typically decreases with depth (Figure 2.4(a)), which leads to the propagation paths in Figure 3.2.

Rays that propagate mainly in the vertical direction experience a lower average sound speed than those propagating more horizontally, since the latter spend more time in the shallow-water region, where the sound speed is higher. Consequently, even when the vertical separation between the ASVs and the AUV remains constant, the differences in the horizontal distances can lead to path-dependent variations in the effective sound speed. This path dependency introduces a range-dependent bias in the estimated distances if a single constant average sound speed is assumed across all measurements. The magnitude of this error increases with the disparity in the horizontal ranges between the ASVs and the AUV.

To account for this effect during localization, this thesis investigates an approach in which the effective sound speed is estimated for each new set of incoming measurements. This approach allows the system to account for path-specific variations in the average sound speed, thus improving robustness and accuracy in complex, real-world environments.

3.2. Multipath Propagation

Another aspect that requires consideration is multipath propagation. When an acoustic signal is transmitted from a hydrophone, it propagates omnidirectionally, which is modeled as a multitude of rays in all directions. These rays can be reflected at the surface or bottom of the ocean or other obstacles in the environment, resulting in multiple propagation paths. This behaviour is illustrated in Figure 3.3 for a horizontal range of 50 m, showing both direct, Line of Sight (LoS), and reflected, Non Line of Sight (NLoS) rays, with the same color scheme as in the ray figures above.

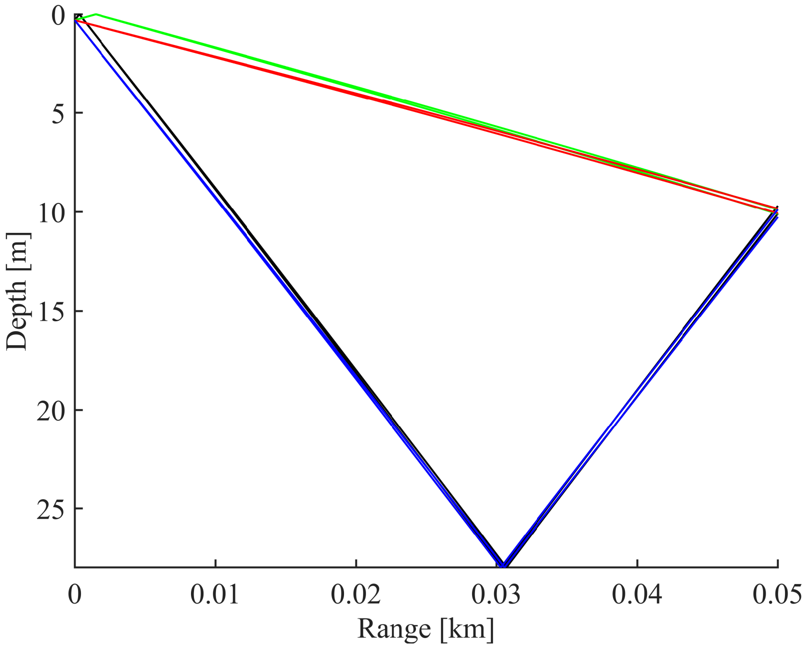

Figure 3.3.: Eigenrays for a horizontal range of 50 m, a sender depth of 0.3 m and a receiver depth of 10 m.

This propagation pattern leads to multiple arrivals at the receiver from a single source. Consequently, the impulse response at the receiving hydrophone is characterized by a sequence of discrete impulses, each corresponding to a different propagation path. The first arriving ray exhibits the highest amplitude, while subsequent arrivals exhibit decreasing amplitudes, which can be contributed to the additional path loss incurred by the longer propagation paths and loss due to reflection (Figure A.1 Appendix A).

The hydrophones employed in this thesis operate at a frequency of 40 kHz providing a temporal resolution of about $\Delta t = \frac{1}{f} = 25\,\mu\text{s}$. Therefore rays arriving with a time difference of at least 25 µs can be resolved, which corresponds to a path length difference of about 3.75 cm for a sound speed of 1500 m/s. For the ranges considered - greater than 9.7 m, corresponding to the AUV depth of 10 m - such a difference is insignificant, and the resolution is therefore sufficient to separate direct and reflected rays. The first-arriving ray is assumed as LoS, therefore it is amplified by the AUV and transmitted back to the corresponding ASV.

3.3. Simulation of Data

For the simulations it is assumed that the channel is time invariant during the measurement period. Moreover, the processing time at the AUV is assumed known and can thus be disregarded. The ASVs are synchronized and RTToF measurements are utilized. Therefore, clock offsets between the AUV and the ASVs are not considered, as only the time delay is of relevance. Two simulation scenarios are considered:
Static Simulation: A static localization scenario, where the AUV is assumed to be stationary during each measurement period. This setup is representative of an initial position estimation using a static localization algorithm. The snapshot data, representing a single set of measurements acquired at one time instance, is used to compute an initial state estimate, which serves as the starting point for dynamic tracking.
Trajectory Simulation: A dynamic scenario, where the AUV follows a trajectory. In practical applications, an iterative filter for trajectory tracking is often initialized using the initial state estimate obtained from the static localization step. This initial estimate is derived from the first snapshot of measurements.
Each scenario is repeated 3000 times with independent noise realizations to obtain statistically reliable results.

3.3.1. Noise Model

The transmission channel is assumed to be AWGN with the noise samples modeled as

$$n_i(d) \sim \mathcal{N}(0, \sigma^2(d)). \tag{3.6}$$

The variance (σ^2) of the RTToF signal is derived from the CRLB for a given Signal-to-Noise Ratio (SNR) (2.22). The linear SNR is computed based on the initial signal energy E_0, the ambient noise PSD N_0 and the path loss A_{PL}

$$\mathrm{SNR}_{\mathrm{lin}} = \frac{E_s}{N_0} = \frac{E_0}{N_0} \frac{1}{A_{\mathrm{PL}}(d)}. \tag{3.7}$$

Since the initial energy of the signal and the ambient noise are assumed constant, the variance of the timing estimation can be expressed as

$$\mathrm{VAR}(\hat{\tau}) \geq \frac{1}{8\pi^2 \frac{E_s}{N_0} \beta^2} = \frac{A_{\mathrm{PL}}(d)}{\mathrm{const.}}. \tag{3.8}$$

The path loss depends on the geometric spreading as well as the signal absorption (2.1). The simulations are based on a short range scenario, where absorption is negligible and spherical spreading applies ($k = 2$). Thus, the path loss simplifies to

$$A_{\mathrm{PL}}(d) = d^2, \tag{3.9}$$

which leads to a linear decrease of $\mathrm{SNR}_{\mathrm{lin}}$ with distance ($\mathrm{SNR}_{\mathrm{lin}} \propto \frac{1}{d^2}$) and consequently a quadratic increase of the variance, resulting in a linear increase of the standard deviation with distance $\sigma_\tau \propto d$.

In the idealized case, the CRLB predicts $\mathrm{VAR}(\hat{\tau}) \geq 0$ for $d \to 0\,\mathrm{m}$. However, in practice this is not achievable, as real systems exhibit a distance-independent error floor caused by synchronization jitter, quantization noise or other effects. Therefore, a more realistic model adds a constant offset term $\sigma_{\tau,0}^2$ to represent this error floor

$$\mathrm{VAR}(\hat{\tau}) \geq \frac{d^2}{8\pi^2 \frac{E_0}{N_0} \beta^2} + \sigma_{\tau,0}^2. \tag{3.10}$$

For the simulations, the standard deviation of the ToF measurements is approximated as a linear increase, ranging from 0.1 m at the transmitter ($d \to 0\,\mathrm{m}$) to approximately 1.01 m at $d = 100\,\mathrm{m}$, which is realistic behaviour for acoustic signals in the underwater channel. This simplified model accurately reflects realistic uncertainty in the underwater acoustic channel. The standard deviation applied in the ToF simulations is illustrated in Figure 3.4 as a function of SNR. Since the results are later evaluated for the total two-way travel distance, the RTToF factor is not shown explicitly here.

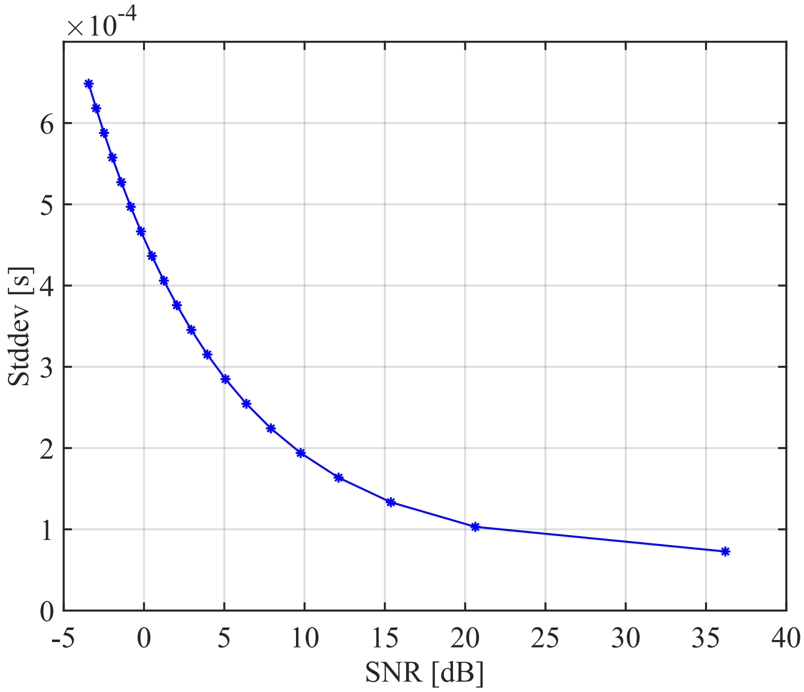

Figure 3.4.: Standard deviation of the simulation data as a function of SNR.

3.3.2. Snapshot Data

For the first static localization scenario, snapshot data is generated using four RT-ToF measurements from the ASVs. The AUV is assumed to be stationary during each measurement period. To evaluate the performance and robustness of the localization algorithms, the AUV is simulated at various, equidistant positions along a diagonal path across the area of interest. This allows for the assessment of position-dependent observability and estimation accuracy.

Additionally, the system is tested at positions outside the bounded area of interest to evaluate the localization performance for non-ideal geometries, as these configurations are relevant for assessing the systems robustness in practical scenarios. This 'outside the area of interest' only refers to the horizontal position, as the vertical position remains unchanged at $-10\,\mathrm{m}$, allowing the evaluation of horizontal drifts. Accordingly, the simulated AUV positions lie at

$\mathbf{r}_\mathrm{a}(x, y) = [\,x,\ y,\ -10\,]^\mathrm{T}\mathrm{m}, \quad x, y \in \{-60 + 15k | k = 0 \ldots 8\}.$

In the static simulation scenarios, the AUV's position in the x-y-plane is collectively referred to as the 'x- and y-position [m]', reflecting the constraint that $x = y$ along the diagonal path. The arrival times are simulated in two different ways. First, using Bellhop, configured for a carrier frequency of $40\,\mathrm{kHz}$ and the representative

SSP (Figure 2.4(a)). Second, by generating the measurements directly according to the measurement function (3.3), assuming a constant average sound speed of 1500 m/s. This allows the evaluation of whether the estimation performance differs significantly when using realistically simulated data from Bellhop compared to idealized measurements generated with the correct analytical model. For both simulation cases, distant dependent noise is added (Section 3.3.1).

3.3.3. Trajectory Data

In a second set of simulations, the AUV is modeled as moving. Since Bellhop is limited to static scenarios and can not simulate time-varying trajectories, the measurements are generated using the measurement (3.5) and a transition model (3.12), that reflect the dynamics of the underwater environment. The state vector at time step n is defined as

$$\mathbf{x}_n = [x_\mathrm{a}, y_\mathrm{a}, z_\mathrm{a}, v_\mathrm{x}, v_\mathrm{y}, v_\mathrm{z}, c]^T, \tag{3.11}$$

where x_a, y_a, and z_a denote the 3D position of the AUV, v_x, v_y and v_z its velocity components, and c the effective average sound speed. The transition from state $\mathbf{x}_{n-1}$ to $\mathbf{x}_n$ is modeled as a stochastic process

$$\mathbf{x}_n = \mathbf{F}\mathbf{x}_{n-1} + \mathbf{B}\mathbf{a} + \mathbf{n}_n, \tag{3.12}$$

which is a standard model employed by DLR. $\mathbf{F}$ denotes the state transition Matrix

$$\mathbf{F} = \begin{bmatrix} \mathbf{I}_3 & (\Delta t - \gamma\frac{\Delta t^2}{2})\mathbf{I}_3 & 0 \\ \mathbf{0}_{3,3} & (1-\gamma\Delta t)\mathbf{I}_3 & 0 \\ \mathbf{0}_{1,3} & \mathbf{0}_{1,3} & 1 \end{bmatrix}, \tag{3.13}$$

$\mathbf{B}$ the control input matrix

$$\mathbf{B} = \begin{bmatrix} \frac{\Delta t^2}{2}\mathbf{I}_3 \\ \Delta t\mathbf{I}_3 \\ \mathbf{0}_{1,3} \end{bmatrix}, \tag{3.14}$$

and $\mathbf{n}_n \sim \mathcal{N}(0, \mathbf{Q}_n)$ the transition noise. The 3×3 identity matrix is denoted by $\mathbf{I}_3$, the 3×3 zero matrix by $\mathbf{0}_{3,3}$ and the 1×3 zero row vector by $\mathbf{0}_{1,3}$. The drag-coefficient $\gamma[s^{-1}]$ is introduced to model hydrodynamic resistance, simulating the deceleration of the AUV due to the high density in water and thereby preventing unrealistic velocity growth. The time step Δt represents the sampling interval between consecutive measurements. $\mathbf{B}$ is the control input matrix for the trajectory of the AUV and $\mathbf{a}$ denotes the direction, in which the AUV is accelerated. The transition noise $\mathbf{n}_n$ is modeled as continuous white acceleration noise, which is integrated over the sampling interval Δt, resulting in a covariance matrix that simultaneously influences the position and velocity of the AUV

$$Q = \begin{bmatrix} \frac{\Delta t^3}{3}\sigma_a^2 & 0 & 0 & \frac{\Delta t^2}{2}\sigma_y^2 & 0 & 0 & 0 \\ 0 & \frac{\Delta t^3}{3}\sigma_a^2 & 0 & 0 & \frac{\Delta t^2}{2}\sigma_a^2 & 0 & 0 \\ 0 & 0 & \frac{\Delta t^3}{3}\sigma_{az}^2 & 0 & 0 & \frac{\Delta t^2}{2}\sigma_{az}^2 & 0 \\ \frac{\Delta t^2}{2}\sigma_a^2 & 0 & 0 & \Delta t^2\sigma_a^2 & 0 & 0 & 0 \\ 0 & \frac{\Delta t^2}{2}\sigma_a^2 & 0 & 0 & \Delta t\sigma_a^2 & 0 & 0 \\ 0 & 0 & \frac{\Delta t^2}{2}\sigma_{az}^2 & 0 & 0 & \Delta t\sigma_{az}^2 & 0 \\ 0 & 0 & 0 & 0 & 0 & 0 & \Delta t^2\sigma_c^2 \end{bmatrix}. \tag{3.15}$$

[20]. Here, σ_a^2 denotes continuous PSD of the acceleration noise in x- and y-direction, $\sigma_{a,z}^2$ in z-direction, and σ_c^2 the corresponding PSD of the noise on the sound speed c. The unit of σ_a is $\mathrm{m}^2/\mathrm{s}^3$, corresponding to the PSD of the acceleration noise.

The AUV trajectory simulations are initialized using a position from the snapshot-based simulations at $\mathbf{r}_\mathrm{a}^{(0)} = [-15, -15, -10]^\mathrm{T}$ with an initial assumed sound speed of 1500 m/s. The vehicle starts from rest, i.e., with an initial velocity of 0 m/s in all directions.

Two simulation sets were considered to investigate the filter behavior under different motion dynamics. In both sets, the AUV followed a pre-planned diagonal trajectory across the area of interest, implemented by applying identical accelerations in the x- and y-directions while maintaining zero acceleration in the z-direction. This predefined motion ensures that the underlying transition model is known to the tracking algorithms. The corresponding measurement data is generated according to the measurement model (3.5).

In both sets, a constant acceleration of $0.5\,\mathrm{m}/\mathrm{s}^2$ is applied in the x- and y-directions, while the acceleration in the z-direction is set to $0\,\mathrm{m}/\mathrm{s}^2$. The process noise is modeled with standard deviations of $\sigma_{x,y} = 0.5\,\mathrm{m}^2/\mathrm{s}^3$ in the horizontal plane for **Set 1** and $\sigma_{x,y} = 1\,\mathrm{m}^2/\mathrm{s}^3$ for **Set 2**. The noise in the vertical direction for **Set 1** and **Set 2** is $\sigma_z = 0.001\,\mathrm{m}^2/\mathrm{s}^3$ to maintain an approximate depth of 10 m. Correspondingly, the damping factors were adjusted to $\gamma_{x,y} = 0.8\,\mathrm{s}^{-1}$ in x- and y-direction and a vertical damping of $\gamma_z = 0.4\,\mathrm{s}^{-1}$ is applied to avoid unintended upward drift due to

the acceleration noise. The trajectory is simulated over a total of 150 time steps. While Bellhop inherently accounts for ray curvature and depth dependent variations of the SSP, these effects must be explicitly modeled in the trajectory simulations. To this end, the previously discussed effective average sound speed is modeled as a dynamic state by adding a small stochastic noise term σ_c^2 to c. Although this approach does not replicate the exact physical effect of the SSP, which assigns an independent different effective average sound speed to each propagation path, it reflects the fact, that the average sound velocity varies with the AUV's position. Thus, a single effective sound speed is applied for all propagation paths simultaneously, which changes depending on the position of the AUV.
Additionally, the LoS condition, which determines, whether a direct acoustic path between the ASV and AUV exists, is dynamically evaluated at each time step. This maximum LoS distance is computed based on the current sender and receiver depths as well as the corresponding SSP (Figure 2.4(a)), ensuring that the model correctly identifies regions where direct acoustic communication between the AUV and the ASVs is limited due to the curvature of the sound rays.

Maximum Propagation Distance Due to Ray Curvature

Due to the curvature of acoustic rays, the horizontal propagation range of direct signals is inherently limited. This limitation depends on the depths of ASVs and the AUV, as well as on the gradient of the SSP. For the simulation of the trajectory data, it is crucial to determine the maximum horizontal distance between the AUV and an ASV beyond which direct communication is no longer possible. To compute this limit, a simplified model with a linearly varying SSP is assumed within the relevant water mass, such that the gradient g of the sound speed is constant. Under this assumption, the ray curvature can be modeled as circular with the radius R given by

$$R = -\frac{c_0}{\cos\gamma_0 \cdot g} \tag{3.16}$$

[14]. Here, c_0 is the sound speed at the transmitter (ASV), γ_0 the initial transmission angle relative to the horizontal, and $g = \frac{\partial c}{\partial z}$ the sound speed gradient (typically negative in shallow waters). Figure 3.5 illustrates the geometric relations governing the acoustic ray propagation.

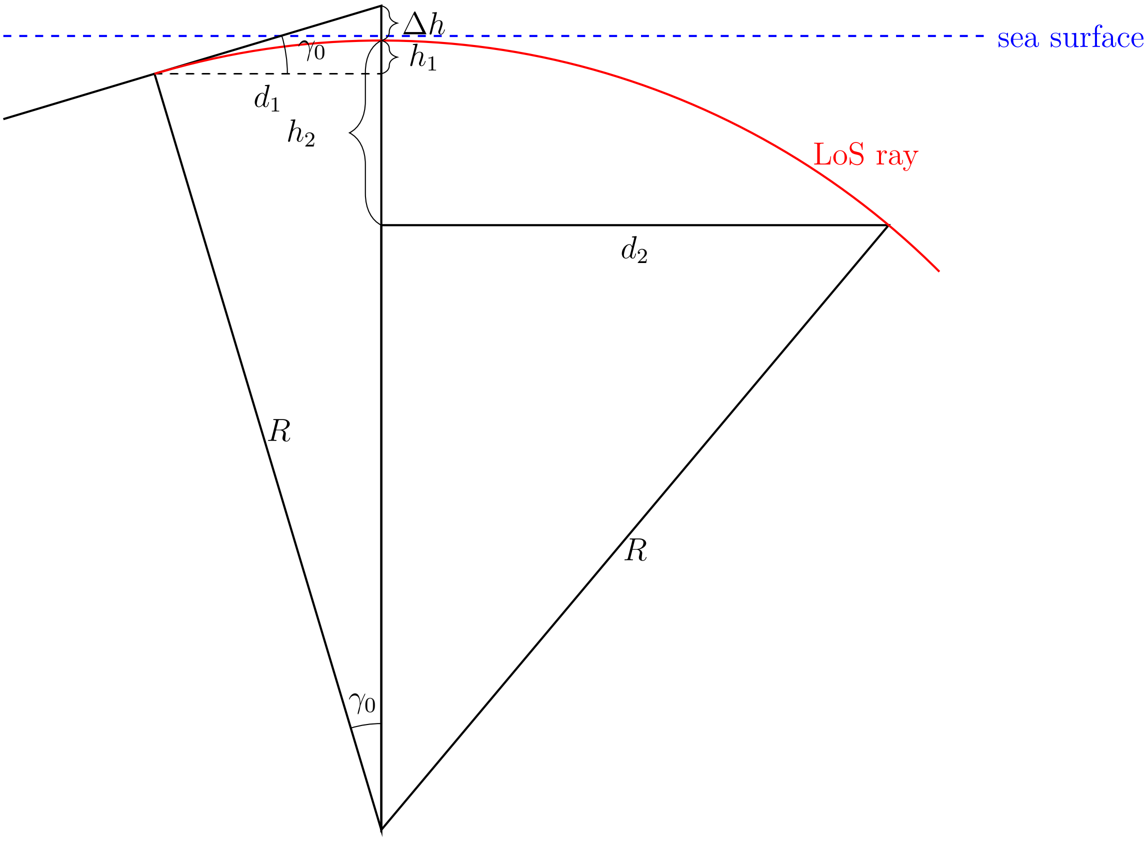

Figure 3.5.: Geometric relations of the acoustic ray propagation underwater.

The red curve represents the bent ray path, determined by the initial angle γ_0 and the dashed blue line the surface of the water. The heights h_1 and h_2 denote the effective depths of the transmitter and receiver respectively. Here, h_1 and h_2 are positive in z- directions, so that a depth of 0.5 m corresponds to $h_1 = 0.5\,\mathrm{m}$. It has to be noted that the figure is not to scale; in reality, the radius R of the curve on which the ray is bent is significantly larger.
For horizontal transmission ($\gamma_0 = 0°$), the maximum horizontal range between the receiver and the transmitter is constrained by the relative depth between the transmitter and receiver

$$d = \sqrt{\left(\frac{c_0}{-g}\right)^2 - \left[\left(\frac{c_0}{-g}\right) - (h_2 - h_1)\right]^2}. \tag{3.17}$$

However, when the signal is launched at a slight upward angle, the ray can propagate farther before bending downward, thereby increasing the horizontal range. The total horizontal distance can be decomposed into two segments $d = d_1 + d_2$, where d_1

denotes the distance traveled while the ray propagates upward, and d_2 the distance traveled while the ray propagates downward.

To determine the largest possible horizontal distance, the maximum send-off angle must be found such that the ray does not reflect at the sea surface:

$$h_1(\gamma_0) = \tan\gamma_0 \cdot d_1 - \Delta h, \tag{3.18}$$

substituting with $\Delta h = \frac{R}{\cos\gamma_0} - R$ and rearranging leads to

$$\begin{aligned} h_1(\gamma_0) = \tan\gamma_0 \cdot \frac{c_0 \cdot \sin\gamma_0}{-g \cdot \cos\gamma_0} \\ - \left[\frac{c_0}{-g \cdot \cos\gamma_0} \cdot \frac{1}{\cos\gamma_0} - \frac{c_0}{-g \cdot \cos\gamma_0}\right]. \end{aligned} \tag{3.19}$$

This results in the final equation

$$h_1(\gamma_0) = \frac{\tan^2(\gamma_0) \cdot c_0}{-g} - \left[\frac{c_0}{-g \cdot \cos^2(\gamma_0)} + \frac{c_0}{g \cdot \cos\gamma_0}\right], \tag{3.20}$$

which can be solved numerically, yielding a maximum launch angle that still allows a direct path to the receiver. The corresponding maximum horizontal distance is then computed by

$$\begin{aligned} d = d_1 + d_2 = \sin\gamma_0 \cdot \frac{c_0}{-g \cdot \cos\gamma_0} \\ + \sqrt{\left(\frac{c_0}{-g \cdot \cos\gamma_0}\right)^2 - \left[\left(\frac{c_0}{-g \cdot \cos\gamma_0}\right) - (h_2)\right]^2}. \end{aligned} \tag{3.21}$$

The maximum range between the transmitter and receiver can be calculated with

$$d_{\text{Euclidean}} = \sqrt{d^2 + (h_2 - h_1)^2}. \tag{3.22}$$

At the given depths for the sender and receiver, no ranges larger than $d_{\text{Euclidean}}$ are possible. Using the linear SSP assumption, the computed ray path closely matches the ray trajectories simulated by Bellhop, which is illustrated in Figure 3.6. This validates the analytical approach for the purposes of this thesis and therefore allows for the evaluation of LoS conditions during trajectory simulations.

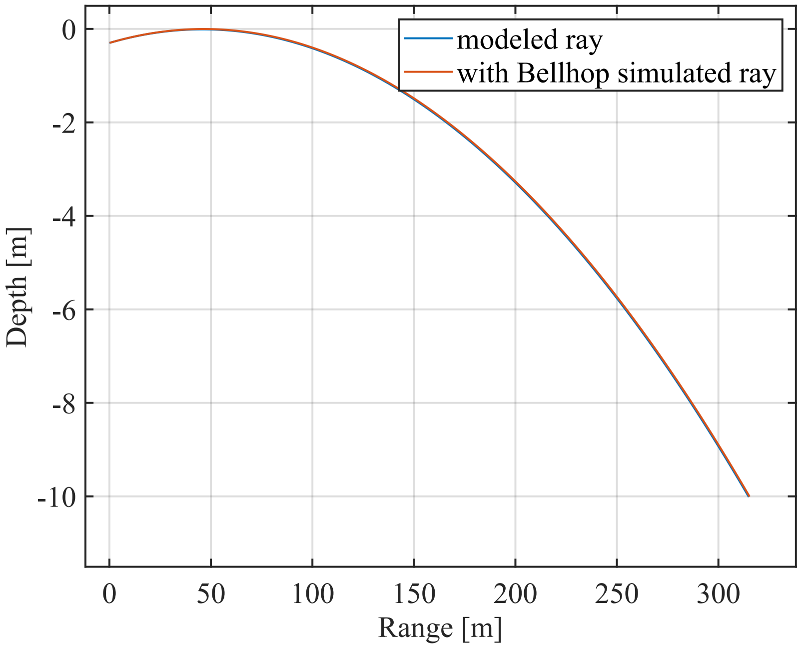

Figure 3.6.: Comparison between approximated ray propagation under the linear sound speed assumption and a ray simulated using Bellhop.

3.4. System Geometry

Since the ASVs are stationary, in a preliminary step their optimal geometric configuration has to be determined. The ASVs are arranged such that three of them form an equilateral triangle, which is known to be favourable for position estimation with three reference points [21]. The fourth ASV, which is needed for the additional estimation of the sound speed, is placed at the center of this triangle, which is aligned with the center of the area of interest.

To determine the optimal side length of the triangle, the CRLB is computed at various positions of the AUV across the area of interest for different triangle sizes. For simplicity, the error introduced by assuming a constant average sound speed is neglected in the CRLB calculations, and it is assumed that the sound speed is identical for all propagation paths. Therefore, the Jacobian of the measurements can be calculated with

$$\mathbf{J} = \begin{bmatrix} \frac{2t(x_a - x_1)}{cd_1} & \frac{2(y_a - y_1)}{cd_1} & \frac{2t(z_a - z_1)}{cd_1} & -\frac{2d_1}{c^2} \\ \frac{2(x_a - x_2)}{cd_2} & \frac{2(y_a - y_2)}{cd_2} & \frac{2(z_a - z_2)}{cd_2} & -\frac{2d_2}{c^2} \\ \vdots & \vdots & \vdots & \vdots \\ \frac{2(x_a - x_i)}{cd_i} & \frac{2(y_a - y_i)}{cd_i} & \frac{2(z_a - z_i)}{cd_i} & -\frac{2d_i}{c^2} \end{bmatrix}, \tag{3.23}$$

where d_i represents the euclidean distance between the AUV and the corresponding ASV$_i$:

$$d_i = \sqrt{(x_a - x_i)^2 + (y_a - y_i)^2 + (z_a - z_i)^2}$$

and the factor 2 is introduced due to the round-trip ranging. The absolute value of the average sound speed does not influence the bound, as it is a multiplicative factor in the calculation that affects both the Jacobian and the covariance matrix equally. The individual variances of the measurements are calculated based on the noise model in Section 3.3.1.

The corner of the area of interest that is farthest from the anchor triangle is selected to determine the optimal sensor geometry. This is due to the fact that the estimation performance is typically worst at the most distant and geometrically unfavorable positions. Consequently, the ASV configuration must ensure robustness even for this setup. Figure 3.7 shows the CRLB for this AUV position as a function of the triangle's side length. The results indicate, that the optimal side length for localization of the AUV is 61 m, where the positioning CRLB is minimized. In contrast, the optimal side length for sound speed estimation differs, but since position accuracy is the primary objective of this work, the configuration is selected based on the minimum CRLB for position estimation. Hence, the positions of the ASVs are defined as

$$\mathbf{r}_1 = [-30.5, 17.6091, -0.3]^{\mathrm{T}}\mathrm{m}, \tag{3.24}$$

$$\mathbf{r}_2 = [30.5, 17.6091, -0.3]^{\mathrm{T}}\mathrm{m}, \tag{3.25}$$

$$\mathbf{r}_3 = [0, -35.2184, -0.3]^{\mathrm{T}}\mathrm{m}, \tag{3.26}$$

$$\mathbf{r}_4 = [0, 0, -0.3]^{\mathrm{T}}\mathrm{m}. \tag{3.27}$$

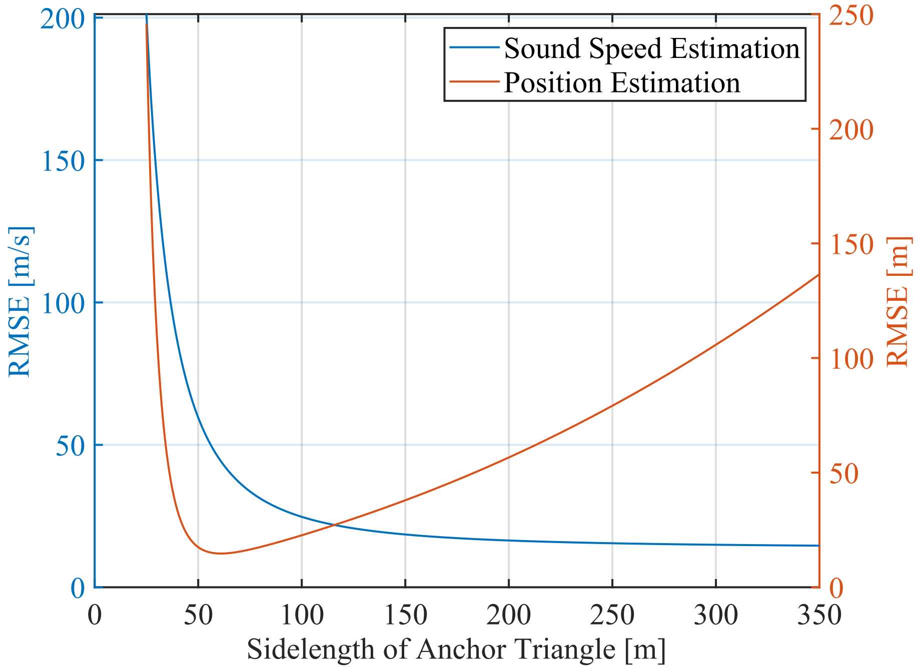

Figure 3.7.: CRLB for different side length of the ASV triangle.

4. Localization Algorithms

This chapter presents various localization algorithms that utilize the RTToF measurements $\boldsymbol{\tau} = [\tau_1, ..., \tau_i]^{\mathrm{T}}$ to localize the AUV.

4.1. Static Methods

First, static estimation techniques used to compute the parameter vector $\boldsymbol{\Theta} = [x_a, y_a, z_a, c]^{\mathrm{T}}$, representing the AUVs position and the average sound speed in water, are outlined.

4.1.1. Maximum Likelihood Estimator

The Maximum Likelihood (ML) estimation is based on an assumed PDF of the observed measurements given the unknown parameter vector $\boldsymbol{\Theta}$ [17]. It determines the parameter vector that maximizes the likelihood function $p(\boldsymbol{\tau}|\boldsymbol{\Theta})$, i.e. the probability that the observed signals τ_i occur, calculated based on the measurement function and the estimated parameters $\hat{\boldsymbol{\Theta}}$

$$\hat{\boldsymbol{\Theta}} = \arg\max p(\boldsymbol{\tau}|\boldsymbol{\Theta}). \tag{4.1}$$

The likelihood is evaluated by comparing the actual measurements τ_i with the model based predictions $\hat{\tau}_i = h_i(\Theta_i)$, obtained from the current parameter estimate. Assuming independent, zero-mean Gaussian measurement noise with the variances σ_i^2, the likelihood of the measurements is given by

$$p(\boldsymbol{\tau}|\boldsymbol{\Theta}) = \prod_{i=1}^{I} \frac{1}{\sqrt{2\pi}\sigma_i} \exp\Big\{-\frac{(\tau_i - \hat{\tau}_i)^2}{2\sigma_i^2}\Big\}. \tag{4.2}$$

Taking the logarithm yields the log-likelihood

$$\ln p(\boldsymbol{\tau}|\boldsymbol{\Theta}) = \sum_{i=1}^{I} \ln \frac{1}{\sqrt{2\pi}\sigma_i} - \sum_{i=1}^{I} \frac{(\tau_i - \hat{\tau}_i)^2}{2\sigma_i^2}. \tag{4.3}$$

The first term is independent of the estimation parameters and can therefore be discarded for estimation. Consequently, the most probable parameters are estimated by maximizing the second part of the sum

$$\hat{\boldsymbol{\Theta}} = \arg\max_{x,y,z,c} - \sum_{i=1}^{I} \frac{(\tau_i - \hat{\tau}_i)^2}{2\sigma_i^2}. \tag{4.4}$$

Thus, for Gaussian measurement noise, maximizing the likelihood function is equivalent to minimizing the sum of the weighted squared residuals. Consequently, the ML estimation corresponds to solving a weighted least-squares problem

$$\hat{\boldsymbol{\Theta}} = \arg\min_{x,y,z,c} \sum_{i=1}^{I} \frac{(\tau_i - \hat{\tau}_i)^2}{2\sigma_i^2}. \tag{4.5}$$

Several numerical optimization techniques can be employed to solve the ML estimation problem.

Iterative Weighted Least Squares

The Iterative Weighted Least Suqares (IWLS) algorithm provides a numerical approach to solve the ML problem for linear or locally linearized problems [17]. It minimises the sum of squared residuals between the measured and predicted observations, incorporating the measurement uncertainty through a weighting matrix derived from the inverse of the measurement covariance matrix. The update equation for a single iteration is given by

$$\hat{\boldsymbol{\Theta}}_{\mathrm{wls}} = (\mathbf{J}^{\mathrm{T}}\mathbf{W}\mathbf{J})^{-1}\mathbf{J}^{\mathrm{T}}\mathbf{W}\tau, \tag{4.6}$$

where $\mathbf{J}$ denotes the Jacobian matrix of the measurements derived at $\mathbf{J} = \frac{\partial h}{\partial \Theta}|_{\hat{\Theta}}$, $\mathbf{W} = \boldsymbol{\Sigma}^{-1}$ the diagonal weighting matrix and $\boldsymbol{\tau}$ the vector containing the observed time delays.

In this thesis the IWLS algorithm is applied to jointly estimate the position of the AUV and the average sound speed using the RTToF measurements.

Linearization via Taylor Expansion In a preliminary step the measurement model (3.5) is linearized around the current estimate Θ. The first-order Taylor expansion [22] leads to

$$\boldsymbol{\tau} \approx \hat{\boldsymbol{\tau}} + \mathbf{J} \cdot (\boldsymbol{\Theta} - \hat{\Theta}) = \mathbf{J} \cdot \boldsymbol{\Theta} + \hat{\boldsymbol{\tau}} - \mathbf{J} \cdot \hat{\boldsymbol{\Theta}}, \tag{4.7}$$

where $\hat{\boldsymbol{\tau}} = h(\hat{\boldsymbol{\Theta}})$ denotes the predicted time delay, based on the current parameter estimate $\hat{\boldsymbol{\Theta}}$. This results in the linearized equation

$$\hat{\boldsymbol{\tau}} - \boldsymbol{\tau} + \mathbf{J} \cdot \hat{\boldsymbol{\Theta}} = \mathbf{J} \cdot (\boldsymbol{\Theta} - \hat{\boldsymbol{\Theta}}) + \boldsymbol{\epsilon}, \tag{4.8}$$

which is in the linear form $\mathbf{y} = \mathbf{A}\mathbf{x} + \boldsymbol{\epsilon}$, with $\mathbf{y} = \boldsymbol{\tau} - \hat{\boldsymbol{\tau}}$, $\mathbf{A} = \mathbf{J}$, and $\mathbf{x} = \boldsymbol{\Theta}$, making it suitable for IWLS estimation. The localization performance of the algorithms is also investigated for AUV positions that fall outside the area of interest; therefore, the estimation problem is potentially ill-posed in these cases. To ensure numerical stability, the Tikhonov regularization [23] is introduced, resulting in a regularized update

$$\hat{\boldsymbol{\Theta}}_{\text{new}} = (\mathbf{J}^{\mathrm{T}}\mathbf{W}\mathbf{J} + \lambda\mathbf{D})^{-1}\mathbf{J}^{\mathrm{T}}\mathbf{W}(\tau - \hat{\tau}) + \hat{\boldsymbol{\Theta}}_{\text{old}}. \tag{4.9}$$

Here, $\hat{\boldsymbol{\Theta}}_{\text{old}}$ and $\hat{\boldsymbol{\Theta}}_{\text{new}}$ denote the parameter estimates before and after the update, respectively, $\mathbf{D}$ a diagonal scaling matrix, which adjusts the regularization strength per parameter and λ a regularization parameter controlling a maximum step size of the estimator for each iteration. This regularization stabilizes the optimization by dampening the gradient steps.

The algorithm proceeds as follows:

1. **Initialization**: Set initial estimates for the AUVs position and sound speed, ensuring, that the z-position is underwater ($z < 0$).
2. **Prediction**: Compute the expected Round Trip Time of Arrivals $\hat{\boldsymbol{\tau}} = h(\hat{\boldsymbol{\Theta}})$.
3. **Jacobian Computation**: Evaluate $\mathbf{J} = \frac{\partial h}{\partial \Theta}|_{\hat{\Theta}}$.
4. **Update**: Applying the regularized Weighted Least Squares update.
5. **Convergence Check**: Repeat steps 2-4 until either the change in $\hat{\boldsymbol{\Theta}}$ falls below a certain threshold or a maximum number of iterations is reached.

Minimum search algorithm

An alternative approach to solve the ML problem is using a predefined nonlinear optimization algorithm, such as MATLAB's fmincon function to search for the minimum. This method directly seeks the parameter vector that minimizes the likelihood cost function using a Quasi-Newton algorithm [24]. In this implementation, the fmincon optimization is further constrained, to ensure that the z-position remains negative.

4.1.2. Maximum A-Posteriori Estimator

Maximum A-Posteriori (MAP) estimation is a Bayesian generalization of ML estimation that incorporates prior knowledge about the parameters to improve estimation accuracy [17]. It determines the parameter values that maximize the posterior probability $p(\boldsymbol{\Theta}|\boldsymbol{\tau})$, which combines the likelihood of the observed data $p(\boldsymbol{\tau}|\boldsymbol{\Theta})$ with the prior distribution of the parameters $p(\boldsymbol{\Theta})$

$$\hat{\boldsymbol{\Theta}} = \arg\max p(\boldsymbol{\Theta}|\boldsymbol{\tau}) = \arg\max_{\boldsymbol{\Theta}} \frac{p(\boldsymbol{\tau}|\boldsymbol{\Theta})p(\boldsymbol{\Theta})}{p(\boldsymbol{\tau})}. \tag{4.10}$$

Since the marginal probability $p(\boldsymbol{\tau})$ of the observation is not dependent on $\boldsymbol{\Theta}$ it can be neglected for the maximization

$$\hat{\boldsymbol{\Theta}} = \arg\max_{\boldsymbol{\Theta}} p(\boldsymbol{\tau}|\boldsymbol{\Theta})p(\boldsymbol{\Theta}). \tag{4.11}$$

Owing to the monotonicity of the natural logarithm, maximizing the product of the likelihood and the prior distribution is equivalent to maximizing their sum in the logarithmic domain

$$\ln\, p(\boldsymbol{\tau}|\boldsymbol{\Theta})p(\boldsymbol{\Theta}) = \ln\, p(\boldsymbol{\tau}|\boldsymbol{\Theta}) + \ln\, p(\boldsymbol{\Theta}). \tag{4.12}$$

In this context, prior knowledge of the sound speed c is represented by a Gaussian distribution with mean of $\mu_c = 1500\,\mathrm{m/s}$ [25] and a standard deviation of $\sigma_c = 30\,\mathrm{m/s}$, reflecting realistic conditions for the sound speed in seawater

$$p(\Theta_c) = \frac{1}{\sqrt{2\pi}\sigma_c} \mathrm{e}^{-\frac{1}{2}(\frac{\hat{c}-\mu_c}{\sigma_c})^2}. \tag{4.13}$$

Since - similarly to the ML estimation - the maximization is invariant to terms that do not depend on the parameters Θ_i they can be omitted from the optimization function

$$\hat{\boldsymbol{\Theta}} = \arg\min_{\Theta} \frac{(\hat{c} - \mu_c)^2}{2\,\sigma_c^2} + \sum_{i=1}^{I} \frac{(\tau_i - \hat{\tau})^2}{2\,\sigma_{\tau,i}^2}, \tag{4.14}$$

which is solved numerically with the fmincon search algorithm under the constraint that the z-position must be negative.

4.2. Dynamic Methods

To track the trajectory of the AUV, two different filters are implemented: a Particle Filter (PF) and an Extended Kalman Filter (EKF), which estimate the state vector $\mathbf{x}_n = [x_\mathrm{a}, y_\mathrm{a}, z_\mathrm{y}, v_\mathrm{x}, v_\mathrm{y}, v_\mathrm{z}, c]^\mathrm{T}$ at each time step. The underlying principle of both methods is the iterative prediction of the next state based on the system dynamics and the correction of this prediction according to the incoming measurements.

4.2.1. Particle Filter

The PF is a sequential Monte Carlo method that approximates the posterior probability distribution of a system's state by using a set of weighted particles [26]. Each particle represents a possible state of the system, and the sum of particles, along with their weights, provides an empirical representation of the full posterior PDF [27]. The particle weights are updated according to the likelihood of the measurements, and resampling is applied to prevent particle degeneracy. This approach allows the PF to adapt to nonlinear system dynamics and non-Gaussian noise.

Particle Filter Algorithm The algorithm for the PF consists of five main steps: initialization, prediction, update, resampling and iteration.

1. **Initialization**: N particles are drawn from the a-priori probability distribution of the state, which reflects the initial uncertainty of the system. This initial distribution is usually based on prior knowledge, often obtained from a static localization, and modeled as a multivariate Gaussian with

$$\mathbf{x}_0 \sim \mathcal{N}(\boldsymbol{\mu}_0, \mathbf{P}_0), \tag{4.15}$$

where $\boldsymbol{\mu}_0$ denotes the a-priori mean and $\mathbf{P}_0$ the corresponding covariance matrix.

Each particle is assigned an equal initial weight:

$$\mathbf{w}_i^{(0)} = \frac{1}{N}, \qquad i = 1, ..., N. \tag{4.16}$$

2. **Prediction**: The next state of each particle is propagated according to the transition model

   $$\mathbf{x}_n = \mathbf{F}\mathbf{x}_{n-1} + \mathbf{B}\mathbf{a} + \mathbf{n}_n.$$

   The resulting PDF is based on both the previous density and the transition model

   $$p(\mathbf{x}_n|\boldsymbol{\tau}_{1:n-1}) = \int p(\mathbf{x}_n|\mathbf{x}_{n-1})p(\mathbf{x}_n|\boldsymbol{\tau}_{1:n-1})\,\mathrm{d}\mathbf{x}_{n-1}, \tag{4.17}$$

   where $p(\mathbf{x}_n|\mathbf{x}_{n-1})$ represents the transition model and $p(\mathbf{x}_n|\boldsymbol{\tau}_{1:n-1})$ the posterior PDF from the previous time step.

3. **Update**: The weights of the particles are updated based on the likelihood of the received measurements

   $$\mathbf{w}_n^{(i)} = p(\boldsymbol{\tau}_n|\mathbf{x}_n)\mathbf{w}_{n-1}^{(i)} \tag{4.18}$$

   and subsequently normalized as

   $$\sum_{i=1}^{N} \mathbf{w}_n^{(i)} = 1. \tag{4.19}$$

   If resampling is performed at every step, the weights of the old particles $\mathbf{w}_{n-1}^{(i)}$ can be omitted.

4. **Resampling**: To prevent particle degeneracy, a new set of particles is drawn in proportion to their normalized weights

   $$p(\mathbf{x}_n|\boldsymbol{\tau}_{1:n}) \propto p(\boldsymbol{\tau}_n|\mathbf{x}_n) \int p(\mathbf{x}_n|\mathbf{x}_{n-1})p(\mathbf{x}_{n-1}|\boldsymbol{\tau}_{1:n-1})\,\mathrm{d}\mathbf{x}_{n-1}. \tag{4.20}$$

   To further counteract particle impoverishment, regularized resampling is applied. The resampled particles are slightly perturbed by adding small, zero-mean gaussian noise

$$\mathbf{x}_n^{(i)} \to \mathbf{x}_n^{(i)} + \epsilon, \qquad \epsilon_n^{(i)} \sim \mathcal{N}(0, \sigma_{res}^2).$$

5. **Iteration**: For each time step, the sequence of the prediction, update and resampling is repeated with every new set of measurements. If no new measurements are available for a longer period, the particles are propagated using solely the transition model to maintain a continuous estimate of the state.

4.2.2. Extended Kalman Filter

The EKF is a deterministic filtering algorithm that extends the classical Kalman Filter to handle nonlinear systems [27]. To this end, the system models are linearized around the current state estimate using the Jacobian matrices of the state transition and measurement functions.

The EKF operates in an iterative two-step process. First the prior state estimate $\hat{\mathbf{x}}_n^-$ and its covariance $\hat{\mathbf{P}}_n^-$ are predicted with the transition model. Afterwards the predictions are corrected using the actual measurements.

The relative influence of the measurements on the state update is incorporated with the Kalman gain, which is determined by the covariance matrices of the transition noise $\mathbf{Q}_n$ and the measurement noise $\mathbf{R}_n$. To ensure consistency between the simulation and the filter, the measurement and transition model for the simulation and the EKF are identical.

Extended Kalman Filter Algorithm

1. **Prediction:** The prior state and covariance are predicted using the transition model with the posterior state and covariance:

$$\hat{\mathbf{x}}_n^- = \mathbf{F}\hat{\mathbf{x}}_{n-1} + \mathbf{B}\mathbf{a} \tag{4.21}$$

$$\mathbf{P}_n^- = \mathbf{F}\mathbf{P}_{n-1}\mathbf{F}^{\mathrm{T}} + \mathbf{Q}_n \tag{4.22}$$

2. **Update:** The predicted prior states are updated with the current measurements. To that end the residual is computed as the difference between the

actual measurements and the predicted measurements ($h(\hat{\mathbf{x}}_n^-)$)

$$\mathbf{r}_n = \boldsymbol{\tau}_n - h(\hat{\mathbf{x}}_n^-). \tag{4.23}$$

The covariance of the residuals is computed as

$$\mathbf{S}_n = \mathbf{H}_n \mathbf{P}_n^- \mathbf{H}_n^{\mathrm{T}} + \mathbf{R}_n, \tag{4.24}$$

with $\mathbf{H}_n = \frac{\partial h}{\partial x}|_{\hat{x}_n^-}$ denoting the Jacobian of the measurement model evaluated at the predicted state. The Kalman gain is obtained from

$$\mathbf{K}_n = \mathbf{P}_n^- \mathbf{H}_n^{\mathrm{T}} \mathbf{S}_n^{-1}. \tag{4.25}$$

Finally, the state and covariance are updated accordingly:

$$\hat{\mathbf{x}}_n = \hat{\mathbf{x}}_n^- + \mathbf{K}_n r_n, \tag{4.26}$$

$$\mathbf{P}_n = (\mathbf{I} - \mathbf{K}_n \mathbf{H}_k) \mathbf{P}_n^-. \tag{4.27}$$

5. Simulation Results and Discussion

This chapter presents and analyzes the results of the performed simulations, focusing on the performance of the different estimation algorithms and the influence of the measurement data sets. The objective is to assess the estimation accuracy and robustness of the proposed methods.
To quantify the estimation performance, the RMSE is used as a benchmark for the quality of the estimator

$$\mathrm{RMSE} = \sqrt{E[||\hat{\Theta} - \Theta||^2]}. \tag{5.1}$$

Although the sound speed and the AUV position are estimated jointly, their respective errors are evaluated individually to assess the overall localization performance. For comparison with the theoretical lower bound the square root of the trace of the CRLB - including its biased and posterior form - is used, as it represents the minimum achievable RMSE of the estimator, such that

$$\mathrm{RMSE}_{\mathrm{crlb,pos}} = \sqrt{\mathrm{tr}(\mathrm{CRLB}(1:3, 1:3)} \tag{5.2}$$

and

$$\mathrm{RMSE}_{\mathrm{crlb,c}} = \sqrt{\mathrm{tr}(\mathrm{CRLB}(4, 4)}. \tag{5.3}$$

5.1. Static Localization

This section presents and discusses the results of the static localization problem. The performance of the Maximum Likelihood and Maximum A-Posteriori estimators is analyzed and compared to the corresponding CRLB and to each other.
Furthermore, potential model mismatches in the ranging model are assessed based on the idealized data set and the more realistic acoustic environment simulated using Bellhop. By comparing localization results derived from both data sets, it is possible to quantify the extent to which deviations from the assumed propagation model affect the estimation accuracy. The outcome of this static evaluation provides

insight into the sensitivity of the estimators to modeling assumptions and serves as a foundation for the subsequent investigation of the dynamic tracking performance.

5.1.1. Maximum Likelihood Estimation Results

First, the performance of the Maximum Likelihood estimator is evaluated to establish a baseline for subsequent comparison with Bayesian estimators. The ML estimation problem is asymptotically unbiased for $N \to \infty$. Therefore, the ML based solvers, Regularized Weighted Iterative Least Squares and fmincon, are evaluated against the classical CRLB for unbiased estimators.

Mapping of Cramer-Rao Lower Bound

Spatial maps of the CRLB are presented to illustrate the theoretical limits of estimation accuracy across a $160\,\mathrm{m} \times 160\,\mathrm{m}$ area, encompassing and extending beyond the defined $120\,\mathrm{m} \times 120\,\mathrm{m}$ region in which the AUV positions are simulated. The minimum achievable RMSE ($\sqrt{\mathrm{CRLB}}$) for position estimation is illustrated in Figure 5.1 , while the corresponding values for sound speed estimation are shown in Figure 5.2. It can be observed that the CRLB for position estimation exhibits a predominantly triangular structure, whereas the CRLB for sound speed estimation appears more spherical.

The positioning CRLB is governed by the directional gradients of the measurements. Within the triangular ASV formation, high geometric diversity causes these gradients to intersect at steep angles, resulting in high Fisher information and therefore a low CRLB. Outside the triangular region, these gradients become increasingly parallel, the intersection angles flatten, consequently the Fisher information decreases and the CRLB enlarges, which results in the triangular pattern.

In contrast, the sound speed acts as a multiplicative factor in the measurement model, affecting only the absolute scale of the RTToF measurements and not their direction. Consequently, the information content related to sound speed depends on the relative differences between the measurements, and not their direction. These differences are largest at the center of the triangular formation, where the measurements from the corner ASVs deviate most strongly from that at the central ASV, resulting in the lowest CRLB. Toward the edges and outside the formation, the RTToF measurements become more similar, which reduces the independent information about the sound speed and therefore increases the CRLB. Consequently, the

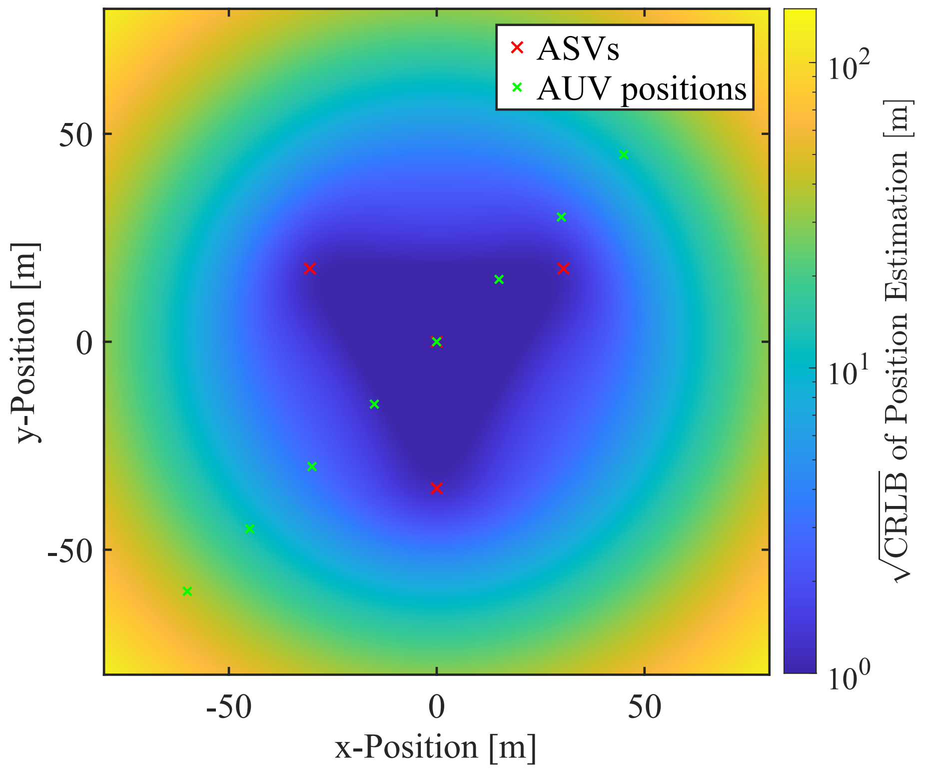

Figure 5.1.: Mapping of the CRLB for position estimation.

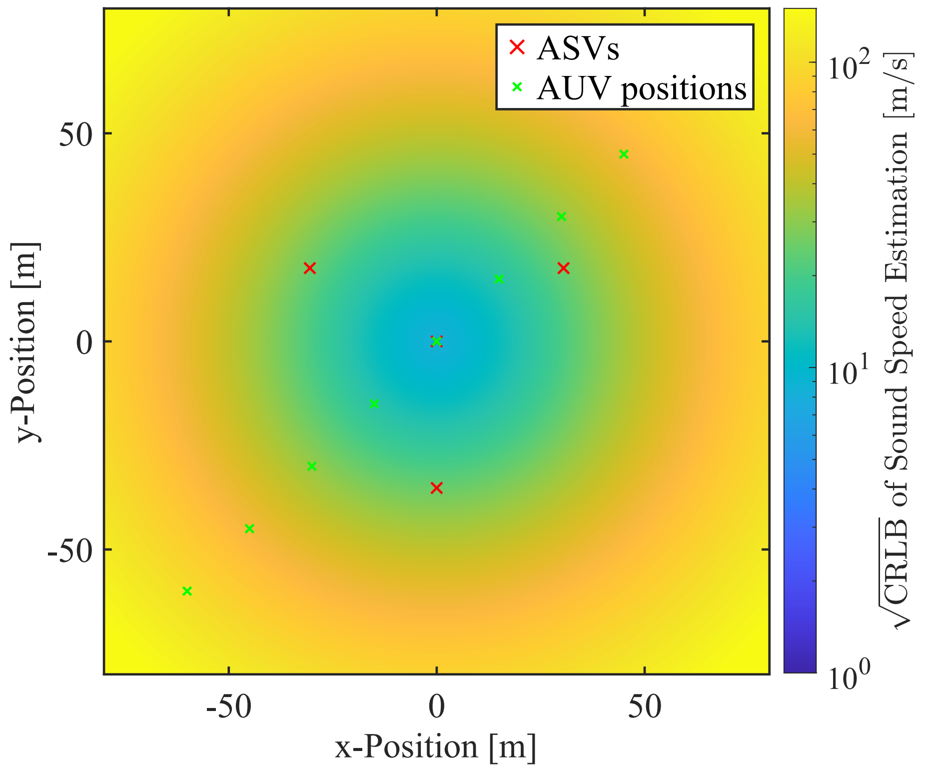

Figure 5.2.: Mapping of the CRLB for sound speed estimation.

resulting CRLB mapping of the sound speed displays a more spherical layout. Both CRLB maps visualize a rapid increase in estimation uncertainty outside the area of interest. This is consistent with the ASV configuration, which was optimized to provide maximum information within the defined area of interest, whereas areas beyond this boundary exhibit unfavourable (or poor) geometry and consequently degraded estimation performance.

Performance of Maximum Likelihood Estimation

The performance of the solvers for the ML estimation problem is evaluated by comparing the RMSE of the estimated parameters to the theoretical CRLB. The RMSE of the position estimates is illustrated Figure 5.3 and the RMSE of the sound speed estimates is depicted in Figure 5.4. Since for the Bellhop-based simulations, the average sound speed across the individual propagation paths differs slightly, the RMSE is computed with respect to the mean sound speed averaged over the four propagation paths.

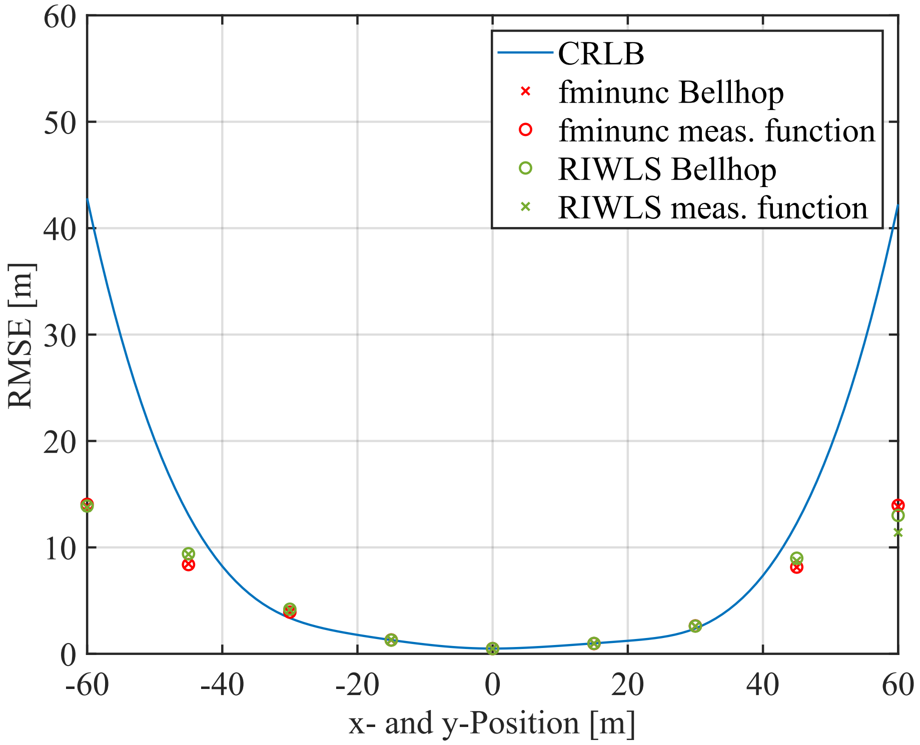

Figure 5.3.: RMSE of the ML estimation of the position.

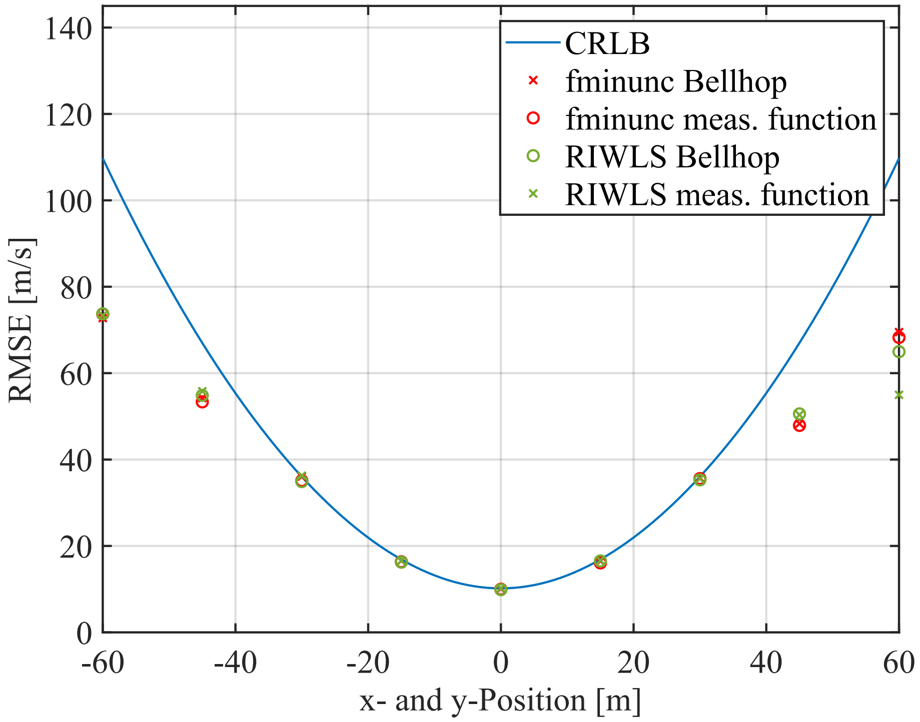

Figure 5.4.: RMSE of the ML estimation of the sound speed.

Both solver algorithms yield consistent results for the data generated with Bellhop and for the idealized data generated based on the measurement model. This indicates that the model mismatch, stemming from the assumption of an identical average sound speed for all propagation paths, has insignificant influence on the estimation performance in this scenario.

Furthermore, both solvers demonstrate similar overall accuracy. In particular, both approach the CRLB for AUV positions within the region $\mathbf{r}_\mathrm{a} = [x_a, y_a, -10]^\mathrm{T}\mathrm{m}$,
$i \in \{-30 + 15k | k = 0, ..., 4\}$.

This behavior confirms that the ML estimation achieves near-optimal performance for the joint estimation of position and sound speed within this region, with the localization RMSE falling below 0.2 m in its central part.

For AUV positions farther outside the area of interest, the RMSE of the ML estimates fall below the theoretical threshold. Since the CRLB represents the minimum achievable RMSE of any unbiased estimator, this behavior indicates that the ML estimator becomes biased in these regions. The bias of the ML estimates is presented in Table 5.1, exemplary shown for the fmincon-based solver using data generated with the measurement model at various AUV positions. The remaining positions exhibit either comparable bias characteristics or no noticeable bias (within the area of interest).

AUV pos. [m]	Bias x [m]	Bias y [m]	Bias z [m]	Bias c [m/s]
-60	2.16	1.97	-1.66	-26.86
-45	0.64	0.54	1.14	-9.20
-30	0.03	0.05	0.70	1.00
-15	0.00	0.00	0.07	0.09
0	0.00	0.00	0.01	0.09

Table 5.1.: Bias of ML estimation for different positions of the AUV.

The results reveal that for AUV positions increasingly distant from the area of interest, the estimates exhibit a systematic deviation from the true parameters. Consequently, the estimator must be regarded as biased in these regions and the classical CRLB is no longer applicable as reference for a minimum achievable RMSE. To further investigate this behaviour, the bias of the solvers is analyzed in more detail.

Bias Analysis

The focus of this section lies on the behaviour of the ML solvers themselves, rather than on discrepancies due to model mismatch between the analytical ranging model and the ranges obtained from the Bellhop simulations.
To analyze the estimator related bias in more detail, the snapshot simulations described in Section 3.3.2 are repeated using a higher spatial sampling along the same diagonal path of the AUV. The simulation data was generated according to the measurement model (3.5) using a constant sound speed of 1500 m/s and distance-dependent noise. The bias of the ML estimates obtained with MATLAB's fmincon solver, based on this data, is illustrated in Figure 5.5. Applying the RWILS algorithm to the same estimation problem results in a similar bias distribution. It can be seen, that as the estimation geometry becomes unfavorable - when the AUV moves farther outside the triangle formed by the ASVs - both the estimated position and the estimated sound speed deviate systematically from their true values. In these regions, the sound speed tends to be underestimated, which increases any position errors since a bias in the sound speed directly propagates into the range estimates. Therefore, the ranges are underestimated ($d = \frac{c\tau}{2}$), which can be seen in the bias curves. In the vicinity of the area of interest, where the geometric resolution in x- and y- direction remains better than in z- direction, the x- and y- position

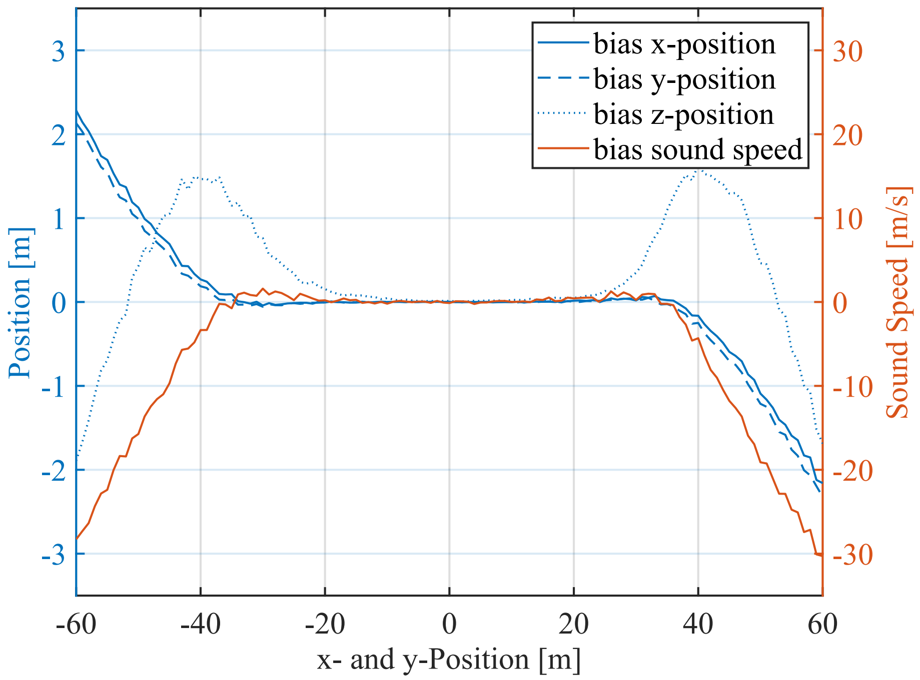

Figure 5.5.: Bias of ML estimation derived with the fmincon solver

of the AUV is only marginally underestimated and z-position is also slightly underestimated. At larger horizontal distances from that area, where the geometric resolution for the horizontal directions declines, the underestimation of the x- and y-position becomes more pronounced, leading to an overestimation of the vertical position. The point-symmetric shape of the horizontal bias curve originates from the coordinate system definition, in which x- and y- position can take both positive and negative values. Thus, for negative positions, a positive bias corresponds to an underestimation, and vice versa.

This systematic bias arises from the ill-conditioning of the estimation geometry which creates flat valleys in the cost function - regions where changes in the estimated parameters result in only small variations of the predicted measurement error, thereby reducing the sensitivity of the optimization. Such valleys are challenging for numerical solvers, fmincon terminates when the step size falls below a specified tolerance and RWILS stops when the parameter updates become sufficiently small or after a fixed number of iterations. Adjusting these convergence thresholds directly influences the resulting bias: lower tolerances generally reduce the bias and increase the variance, while higher ones increase the bias. However, reaching the global minimum is hindered by numerical limitations, as the cost function becomes excessively flat in the vicinity of the optimum [28]. In both cases, premature termination leads to convergence toward locally stable but biased solutions. The regularization inherent to RWILS stabilizes the numerical solution but can also amplify this effect by overly constraining the parameter space, making the algorithm less suitable for this type of estimation problem.

To account for this bias, the Biased Cramér Rao lower bound (BCRLB) is computed as a lower error bound with

$$E\{\Theta - \hat{\Theta}\} \geq b_i^2(\Theta) + \{[\mathbf{I} + \nabla_\Theta(\mathbf{b})]\mathbf{FIM}^{-1}[\mathbf{I} + \nabla_\Theta(\mathbf{b})]^T\}_{ii}.$$

Here, the vector $\mathbf{b}$ contains the bias function of the 3D position and the sound speed

$$\mathbf{b} = [b_x(\Theta), b_y(\Theta), b_z(\Theta), b_c(\Theta)]^T.$$

Consequently, at each point of evaluation, the absolute bias and the Jacobian Matrix

$$\nabla_\Theta(\mathbf{b}) = \begin{bmatrix} \frac{\partial b_x}{\partial x} & \frac{\partial b_x}{\partial y} & \frac{\partial b_x}{\partial z} & \frac{\partial b_x}{\partial c} \\ \frac{\partial b_y}{\partial x} & \frac{\partial b_y}{\partial y} & \frac{\partial b_y}{\partial z} & \frac{\partial b_y}{\partial c} \\ \frac{\partial b_z}{\partial x} & \frac{\partial b_z}{\partial y} & \frac{\partial b_z}{\partial z} & \frac{\partial b_z}{\partial c} \\ \frac{\partial b_c}{\partial x} & \frac{\partial b_c}{\partial y} & \frac{\partial b_c}{\partial z} & \frac{\partial b_c}{\partial c} \end{bmatrix} \tag{5.4}$$

of the bias functions need to be determined.

Since the bias originates from the solver itself and cannot be derived analytically, its approximate deviation and absolute value are obtained by fitting curves to empirically observed bias values. This approach may lead to small inaccuracies in the approximation, resulting from imprecision in the locally fitted bias parameters.

In Figure 5.6, the resulting approximated BCRLB together with the ML position estimation results are illustrated, showing that outside the area of interest, the biased bound lies significantly below the classical CRLB. In Figure 5.7 analogous results for the sound speed estimation are presented, showing a similar trend.

The observed RMSE of both position and sound speed estimation remain below the classical CRLB but align well with the BCRLB, confirming that the solvers exploit bias-related information due to convergence in flat likelihood valleys, exhibiting a smaller variance for the biased case. This relationship is reflected in the BCRLB formulation (2.39), where the additional term couples the gradient of the bias function with the CRLB. Consequently, certain tendencies of the bias function effectively decrease the variance of the estimation.

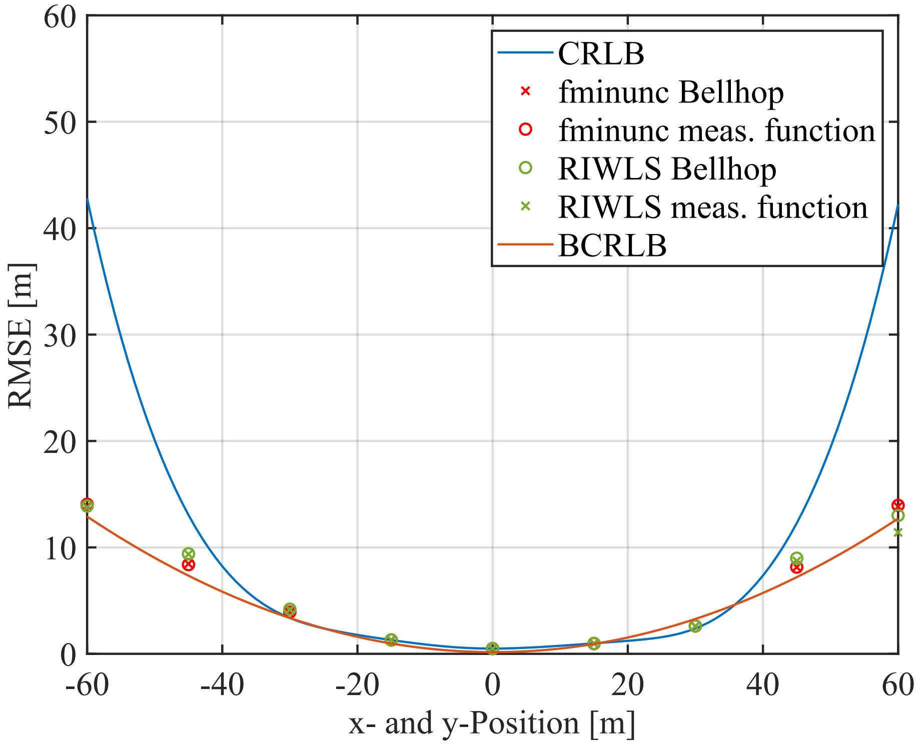

Figure 5.6.: RMSE of ML estimation of the position with the approximated BCRLB.

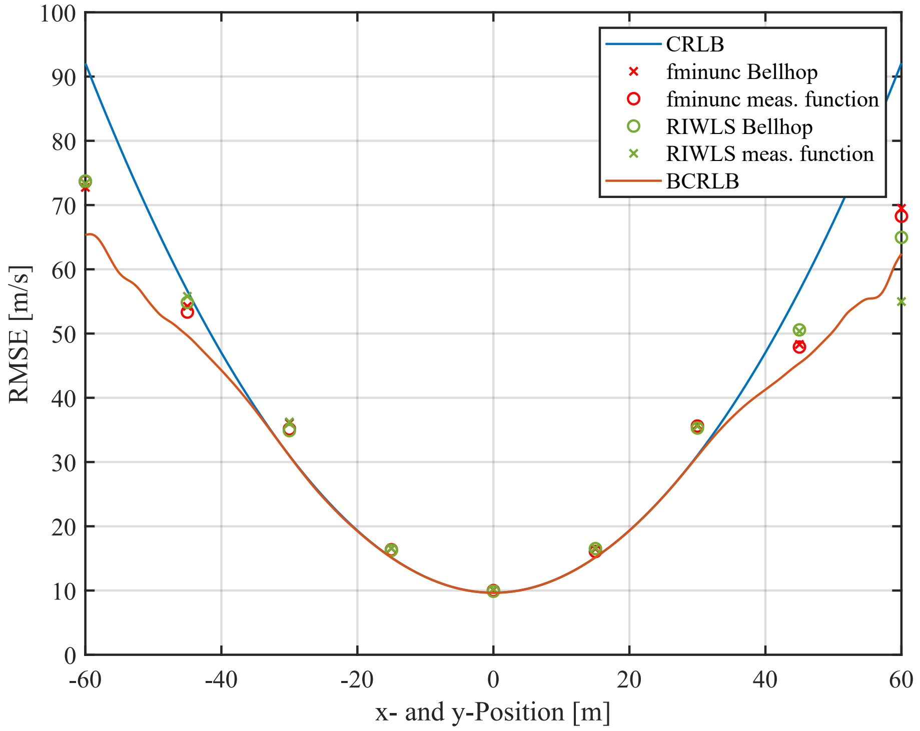

Figure 5.7.: RMSE of Maximum Likelihood estimation of the sound speed with with approximated BCRLB.

5.1.2. Maximum A-Posteriori Estimation Results

In the following, the performance of the Maximum A-Posteriori (MAP) estimation is analyzed to assess the impact of prior information on localization accuracy. The MAP estimation problem was solved using MATLAB's optimization function fmincon under the constraint that the z-position has to be negative. In the following, this method is referred to simply as the MAP estimator.

The performance of the MAP estimator is evaluated by comparing the achieved RMSE with the corresponding CRLB, which in this case includes the a-priori information about the sound speed (2.37). As shown previously for the ML estimation, the unfavourable geometry for AUV positions located farther outside the area of interest can lead to biased estimation results. To account for this, the biased CRLB is approximated analogous to the procedure used for the ML case, with the key difference, that the BCRLB now incorporates the prior information:

$$E\{\Theta - \hat{\Theta}\} \geq b_i^2(\Theta) + \{[\mathbf{I} + \nabla_\Theta(\mathbf{b})][\mathbf{FIM}_{\text{meas}} + \mathbf{FIM}_{\text{prior}}]^{-1}[\mathbf{I} + \nabla_\Theta(\mathbf{b})]^T\}_{ii}. \quad (5.5)$$

It should be noted that again the BCRLB is approximated based on the numerically obtained bias curves since they cannot be derived analytically. Consequently, the presented BCRLB does not represent the exact theoretical RMSE, but provides an approximation that reflects the expected behavior of the MAP estimation.

The RMSE of the MAP-based position estimates, together with the corresponding CRLB and BCRLB, is depicted in Figure 5.8. The results indicate that within the area of interest the position estimation accuracy for both the data sets - simulated with Bellhop and with the measurement model - is nearly identical and both approach the CRLB. Therefore, within the area of interest the model mismatch between the analytical measurement model and the Bellhop-simulated data is inconsequential, which coincides with the findings of the ML estimation. For less favorable geometries, the RMSE of the estimations converges towards the BCRLB, which decreases in those regions. This indicates that under poor geometric conditions, the estimator exhibits reduced variance as a result of bias in the estimates. For the positions located farthest from the center of the area, the results based on the analytical measurement model exhibit a lower RMSE (approximately 1 m less) than those obtained with the Bellhop-simulated data, indicating that for unfavourable conditioning, the data set generated with Bellhop exhibits slightly worse localization performance.

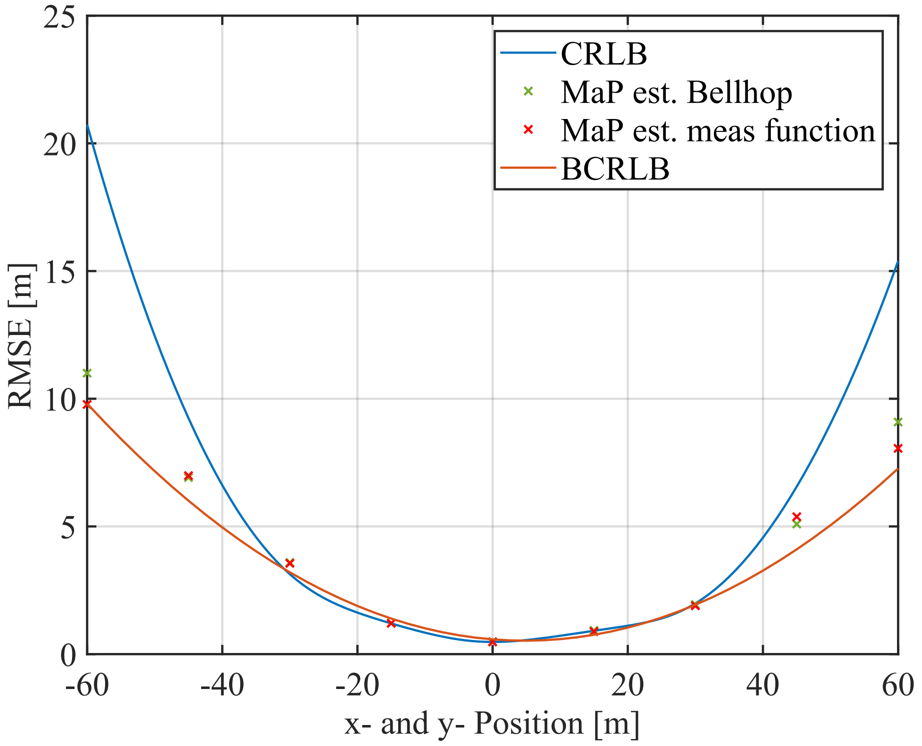

Figure 5.8.: RMSE of the MAP estimation of the position.

In Figure 5.9 the RMSE of the MAP estimator for sound speed estimation is illustrated, which shows a distinctly different behaviour compared to the CRLB. For increasingly poor geometric conditions, the BCRLB decreases strongly, while the classical CRLB asymptotically approaches the a-priori knowledge. The RMSE obtained from the idealized data follows the BCRLB, again demonstrating that under such conditions, the estimator exhibits reduced variance due to the premature termination of the optimization, effectively introducing a bias. The approximated BCRLB, however, lies slightly below the actual RMSE of the estimator, as the influence of the prior information in flat-valley regions of the cost function can lead to an overestimation of the bias gradient and thus an underestimation of the bound.
In contrast, the RMSE of the Bellhop-based estimation increases with larger distances of the AUV from the center, reaching a maximum value of approximately 25 m/s at the position $\mathbf{r}_\mathrm{a} = [-60, -60, -10]^\mathrm{T}\mathrm{m}$.
The deviations in position and sound speed estimation across the various measurement sets are caused by the differing bias tendencies between the two data sets, which can be attributed to the influence of the prior knowledge.

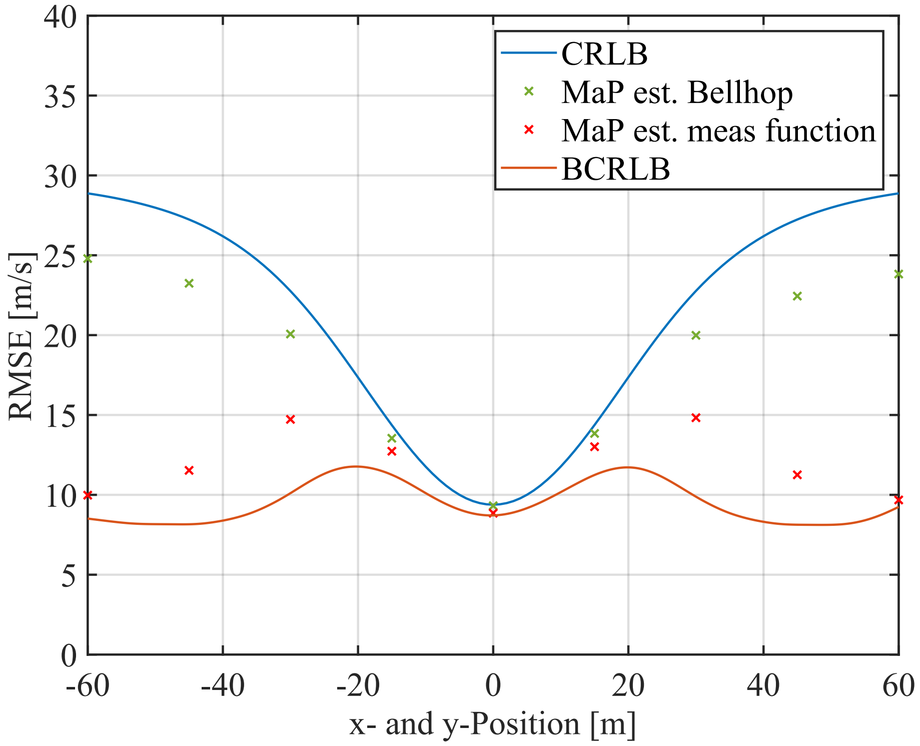

Figure 5.9.: RMSE of the MAP estimation of the sound speed.

Influence of A-Priori Information

To examine this effect in more detail, the bias of the MAP estimation is shown in Table 5.2 for both data sets at positions $\mathbf{r}_\mathrm{a} = [x_\mathrm{a}, y_\mathrm{a}, -10]^\mathrm{T}\mathrm{m}, \quad i \in \{-60, -45, -30\}$. For the idealized measurement data, the bias is minor, with a maximum deviation of $-3.56\,\mathrm{m/s}$ for the sound speed estimation and $-0.73\,\mathrm{m}$ for position estimation. Similar to the ML estimation, this bias originates from unfavorable geometry at AUV positions located outside the area of interest, where the cost function exhibits a flat gradient valley.

Data	AUV pos. [m]	Bias x [m]	Bias y [m]	Bias z [m]	Bias c [m/s]
Bellhop	-60	1.89	1.78	-3.77	-23.27
ideal	-60	0.73	0.49	-0.17	-3.56
Bellhop	-45	1.10	1.05	-0.89	-20.18
ideal	-45	0.30	0.17	1.14	-2.05
Bellhop	-30	0.34	0.39	0.65	-13.82
ideal	-30	0.04	0.01	0.52	-0.13

Table 5.2.: Bias of MAP estimation for data simulated with Bellhop and idealized data.

In these regions, the estimator converges prematurely before reaching the global minimum. These bias tendencies for the idealized data set resemble those observed for the ML estimation, although the scale is smaller: the sound speed tends to be underestimated, leading to a systematic underestimation of the ranges.
For the Bellhop-simulated data, the bias for unfavourable geometry is significantly larger. This behaviour is primarily caused by the prior knowledge used in the MAP estimation, defined as $\mu_c = 1500\,\mathrm{m/s}$ and $\sigma_c = 30\,\mathrm{m/s}$, which represent the expected average sound speed in shallow waters without information about environmental conditions. The SSP used for the Bellhop simulations (Figure 2.4(a)), corresponds to conditions in August and therefore exhibits higher sound speed of approximately 1522 m/s in the near surface layers (upper 10 m), mainly due to elevated temperature. Consequently, the average sound speed increases, especially for larger horizontal distances. This discrepancy between prior mean and true sound speed has only a minor effect for favourable geometry, since the high Fisher information provided by the measurements dominates the estimation. However, as the geometry becomes less favourable, the estimation increasingly relies on the prior, drawing the sound speed estimate toward its mean value of 1500 m/s and thereby introducing an additional bias in the estimate. This bias subsequently propagates into the position estimates and is particularly pronounced in the z-direction, since the ASVs are located within a single horizontal plane and errors in the sound speed estimation translate most strongly in to the vertical component. Consequently, the bias in z-direction reaches values of up to $-3.77\,\mathrm{m}$ at $\mathbf{r}_\mathrm{a} = [-60, -60, -10]^\mathrm{T}\mathrm{m}$.
The influence of the prior knowledge on the bias can be further examined by considering the geometric relations of the measurement setup.

Geometric Interpretation

In three-dimensional range-based localization, each RTToF measurement between the AUV and an ASV defines a sphere centered around the ASV, with radius proportional to the assumed sound speed and the measured RTToF. The measurement noise turns each sphere into a finite-thickness spherical layer, where the volume of the noise corresponds to the thickness of the layer. The true AUV position lies within the common intersection of all layers. Because of their finite thickness, this intersection is a region rather than a single point and represents the estimation uncertainty. Under poor geometry - e.g., when the ASVs are clustered on one side - the spheres intersect at shallow angles and the intersection area expands into an elongated, approximately ellipsoidal volume. If the sound speed is jointly estimated, it scales all radii proportionally, introducing an ambiguity that is coupled with the position. This coupling amplifies the uncertainty of both position and sound speed, especially under unfavorable geometry.

The introduction of prior knowledge about the sound speed stabilizes the estimation process in such geometrically weak regions. The prior effectively constrains the sphere radii, reducing the ambiguity between position and sound speed. As a result, both the position and sound speed estimates become more stable. However, the MAP estimate of the sound speed tends to be drawn toward the prior mean, introducing a bias when the prior deviates from the true value. Under favorable geometry, the high information content of the measurements dominates the prior, and the MAP estimator remains practically unbiased even for a slightly inaccurate prior mean.

5.1.3. Comparison

Within the area of interest, the results obtained with the MAP estimator closely resemble those of the ML estimator, as the high Fisher information provided by the measurements dominates the estimation. Outside this region, the MAP estimates of both simulation sets exhibit improved performance compared to the ML estimator, with the idealized data yielding an even smaller bias and RMSE. This indicates that the degree of improvement strongly depends on the accuracy and strength of the prior information.

While the ML estimator suffers from diverging position and sound speed estimates under weak geometry, the MAP estimator remains more stable and produces significantly lower bias based on the coupling of sound speed estimation and range estimation for poor system geometry. However, the overall bias of the MAP estimator inherently depends on the nature and accuracy of the a-priori information. Stronger or more informative priors can mitigate the coupling bias arising from ill-posed estimation conditions, but they may simultaneously introduce a systematic bias reflecting the assumptions embedded in the prior itself.

Thus, the MAP estimation provides a robust trade-off between bias and stability. It provides almost bias free estimates under well-conditioned geometry and maintains higher stability in weak geometric conditions due to the softly bounded sound speed assumption, with well-chosen priors leading to improved overall accuracy.

5.1.4. Model Mismatch Concerning Sound Speed

The ranging model assumes an effective average sound speed for all simultaneously incoming measurement paths. In the present scenario, this assumption results in negligible model mismatch for the ML and MAP estimations. The extent of this model mismatch depends on the propagation geometry. Differences in the effective average sound speed increase with the horizontal range between the ASVs and the AUV. For relatively closely spaced ASVs, as in the current setup, the variations are minor, but for larger horizontal separations, these discrepancies become more pronounced. The simulations with Bellhop reveal that for direct vertical propagation (AUV located directly under an ASV), the average sound speed is 1501.2 m/s, whereas for the farthest horizontal range of about 100 m, it increases to 1522.4 m/s. This confirms the assumption, that the average sound speed increases for larger horizontal distances and indicates that too large spacing between ASVs may lead to a measurable model mismatch, when assuming a constant average sound speed for all propagation paths. This indicates that without a correction factor for the different RTToF measurements, which accounts for path-dependent variations in the sound speed, the vehicles in a swarm should avoid overly large spacing.

The bias exhibited by the MAP estimation does not originate from model mismatch but from inaccurate prior information. Incorporating environmental knowledge - such as seasonal effects (e.g., higher sound speed in summer), or typical conditions in oceanic and coastal regions - into the prior information could mitigate this bias and further improve the estimation accuracy.

5.2. Trajectory Tracking

This section presents the results of the filters applied in the trajectory tracking simulations, extending the previous static localization analysis to the case of a moving AUV. Both tracking algorithms - the EKF and the PF - are evaluated over 150 time steps, corresponding to a total simulation duration of the AUVs trajectory for 75 s. Two of the simulated trajectories in the x-y plane are illustrated in Figure 5.10. The blue trajectory correspond to **Set 1**, with an according horizontal acceleration noise of $\sigma_{x,y} = 0.5\,\mathrm{m}^2/\mathrm{s}^3$ and the green one to **Set 2**, with a noise of $\sigma_{x,y} = 1\,\mathrm{m}^2/\mathrm{s}^3$.

The resulting trajectories reflect the influence of the applied acceleration noise, with the trajectory of **Set 2** exhibiting stronger perturbations. The average AUV position over all trajectory simulations after the 150 simulated time steps for both

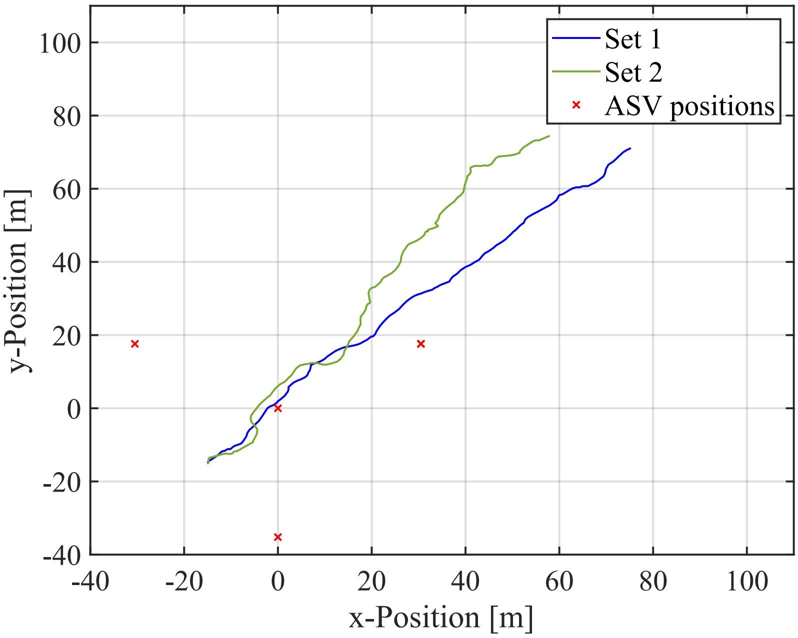

Figure 5.10.: Exemplary trajectories of simulation **Set 1** and **Set 2**.

simulation sets is $\mathbf{r}_\mathrm{a} = [68, 68, -10]^\mathrm{T}$m. The dampening factor in z-direction, which prevents upward drift of the AUV, leads to a minimum depth of approximately 8 m in the simulation data. Based on the calculation for the maximum LoS distance derived in Section 3.3.3, this corresponds to a maximum horizontal range of 254 m for the given sender depth of 0.3 m, using the simplified model of the SSP in Figure 2.4(a). Consequently, the AUV remained within the LoS connectivity region throughout all simulated time steps.

5.2.1. Evaluation of Filter-Based Localization Performance

The localization performance of both filters is evaluated by comparing the RMSE of the position estimation with the minimum achievable RMSE presented by the PCRLB. The performance of the EKF and PF for simulation **Set 1** and **Set 2** are illustrated in Figure 5.11. Both filters were initialized with the results from the snapshot estimation, at position $\mathbf{r}_\mathrm{a} = [-15, -15, -10]^\mathrm{T}$m. A similar tendency can be observed for both filters. At the beginning of the trajectory (approximately the first 10 time steps), the position estimates of both the PF and the EKF improve significantly. This increase in accuracy is due to the filters benefiting from both the accumulation of new measurements and the more favourable measurement geometry in the initial stages.

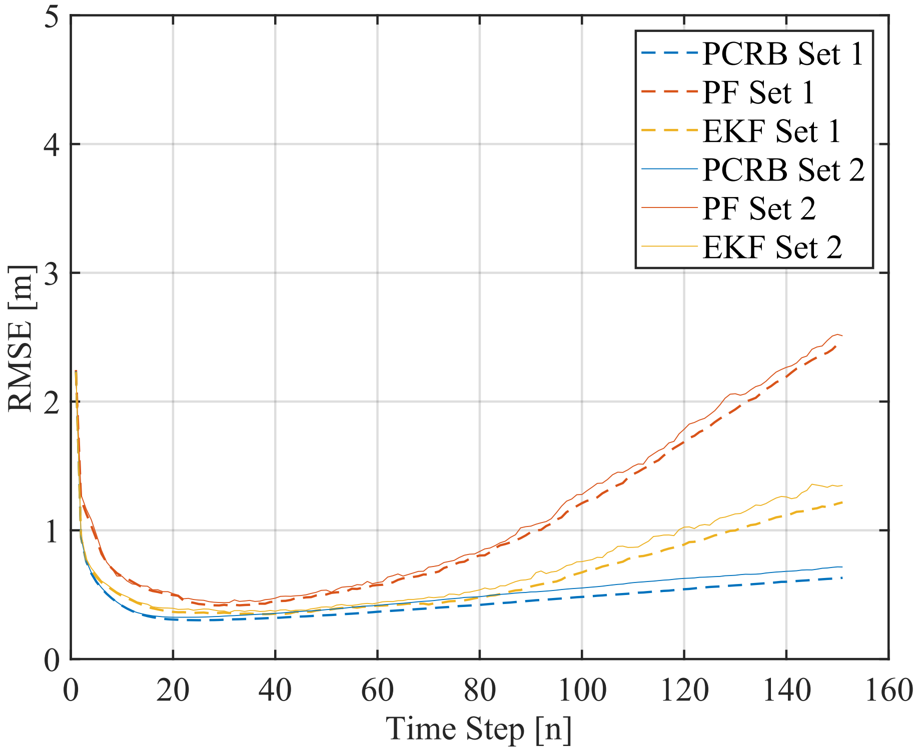

Figure 5.11.: Localization performance of the EKF and the PF for simulation **Set 1** and **Set 2**.

Subsequently, up to approximately time step 30, the estimation improves more gradually, as the additional information gain after the initial steps decreases. Afterwards, a slight increase in the RMSE is apparent, which coincides with the AUV leaving the center of the ASV triangle, which exhibits the best geometric conditioning. Beyond approximately 90 time steps, both filters begin to deviate noticeably from the PCRLB, which continues to increase at a similar rate. This behaviour occurs as the AUV reaches an average position of $\mathbf{r}_\mathrm{a} = [32, 32, -10]^\mathrm{T}\mathrm{m}$ across all simulated trajectories, corresponding to the onset of the region with increasingly poor geometry where the system becomes less well-conditioned. The divergence of the filters is therefore consistent with the problems of unfavourable geometry, which is further discussed in Section 5.2.3.

Comparing the RMSEs of the simulation **Set 1** and **Set 2**, allows an assessment of the impact of the increased acceleration noise. Once the AUVs average position over the simulation trajectories moves beyond the center of the area of interest, the PCRLB for the simulation **Set 2** displays slightly higher values, reflecting the greater uncertainty in the transition model. Both filters exhibit similar performance trends, as the relative differences between each filters RMSE values and the corresponding PCRLB remains nearly identical for both simulation sets. This indicates that neither filter is significantly affected by the increased transition noise. The absolute RMSE difference between **Set 1** and **Set 2** remains below 0.2 m, indicating that the heightened transition noise has negligible impact on the localization performance.

A direct comparison between the two filters reveals that the EKF generally achieves slightly lower RMSE values than the PF across both simulation sets. This difference is likely related to sub-optimal parameter tuning rather than to fundamental limitations of either algorithm.

Each filter offers distinct advantages. The PF provides increased flexibility through parameter tuning, such as adjustable resampling noise and scheme, or the option to broaden the likelihood function, making it more robust under uncertain conditions but potentially leading to suboptimal performance if tuned incorrectly. Since it approximates the posterior PDF of the different parameters, it can adapt to non-Gaussian distributions. In addition, particularly in localization scenarios, the visualization of the particle cloud can be highly informative for diagnosing issues in the filter implementation or in the underlying measurement or simulation setup.

A drawback of the PF is its higher computational complexity, since all particles must be propagated and weighted at each time step. Moreover, due to the stochastic nature of the algorithm and the finite number of particles used, its convergence is not deterministic.

In contrast, the EKF is a deterministic filter that remains computationally efficient and performs reliably under well-defined motion models, making it advantageous for real-time applications with limited processing resources. However, the EKF relies on local linearization of the nonlinear measurement model, which can introduce estimation errors, when the nonlinearity of the model comes more pronounced, (for example at very small distances between the ASV and the AUV). Moreover, since the EKF operates solely based on the predefined transition and measurement model, it lacks the flexibility to adapt internal parameters for increased robustness.

Overall, both filters exhibit consistent qualitative behavior, indicating that the estimation performance is primarily governed by the measurement geometry rather than by the specific filter structure. Consequently, both filters are well suited for the considered localization problem. The choice of the filter is therefore based on the specifications of the problem.

5.2.2. Impact of Sound Speed Estimation

To analyze the impact of the sound speed estimation on the filter performance, the RMSE of the estimated sound speed and the corresponding PCRLBs for both data sets are illustrated in Figure 5.12. It can be observed, that the sound speed estimation for both filters approaches the PCRLB, without diverging for regions of unfavourable geometry. This indicates, that the sound speed estimation does not have a negative impact on the localization performance for bad geometry.

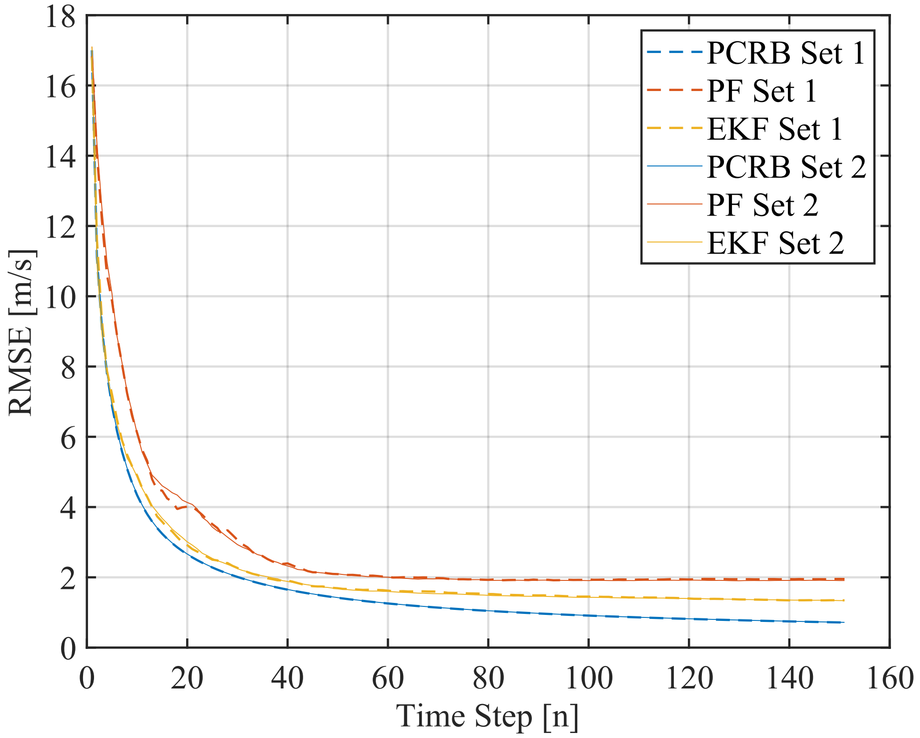

Figure 5.12.: Performance of sound speed estimation of the EKF and the PF for simulation **Set 1** and **Set 2**.

To validate this assumption, an EKF was implemented for the case of a known sound speed for simulation **Set 1**. Figure 5.13 includes the localization performance of this EKF. It can be observed, that the trend of the localization performance is the same when the sound speed is known, which confirms that the deviations between the filters and the PCRLB are not caused by the joint estimation of position and sound speed.

This behavior arises because the transition model for the sound speed allows only small variations, representing slow environmental fluctuations in the effective sound speed. Consequently, the associated process noise is minor, and errors introduced by slightly inaccurate sound speed estimates remain limited, as the model inherently constrains large deviations. If the initial sound speed estimate is sufficiently accurate, its impact on the range estimates is minimal. Therefore, the coupling between sound speed and position estimation, which has previously shown to induce bias in the static case under unfavorable geometry, has only a negligible effect in the filter-based trajectory tracking when the initial geometry is favorable.

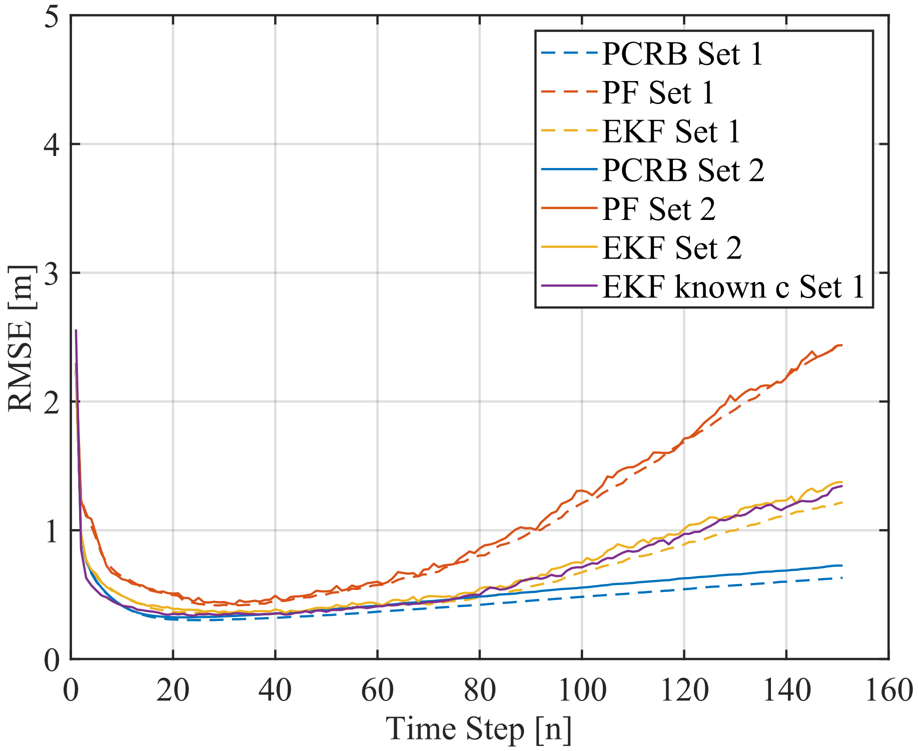

Figure 5.13.: Localization of the EKF and the PF for simulation **Set 1** and **Set 2**, including the EKF for the case of known sound speed for **Set 1**.

However, if the initial sound speed estimate is biased due to an unfavorable initial geometry and this bias is not reflected by a sufficiently large initial uncertainty, the error tends to persist over time. Because the transition model typically assumes low process noise, only limited correction can occur at each time step. In such a case, a PF would be preferable, as an increased resampling noise for the sound speed could help mitigate this incorrect initial estimate and enable faster convergence toward the true value, although the overall performance would still remain suboptimal.
Furthermore, if the estimated sound speed only remains within a reasonable range because of the restrictive transition model rather than due to informative mea-

surements, its relevance for the estimation under unfavourable system geometry is questionable. In such cases, the sound speed estimate is unlikely to provide additional useful information and the localiztaion performance will not be improved by this estimation.

This illustrates once more the importance of geometric conditioning. If the initial geometry is unfavorable, the filter will struggle to correct biased sound speed estimates which would automatically influence the range estimates. Therefore, especially initializing the localization in regions with favorable geometry is crucial for accurate and stable sound speed estimation.

5.2.3. Deviation from the PCRLB

The deviations of the filter performance from the PCRLB primarily originate from the intrinsic limitations of the filtering process rather than from a bias introduced by the coupling between sound speed and position estimation. When the information from the measurements becomes insufficient, the filters increasingly rely on the transition model, which leads to a noticeable divergence from the theoretical lower bound. This can be attributed to poor geometric conditions, under which the directional gradients of the measurements become highly similar, resulting in only a minor information gain.

For the PF, which can assign wrong weights when the positioning geometry is unfavourable, this effect can be visualized. A particle with a biased velocity estimate can still obtain a high weight due to measurement noise, allowing the error to persist over several iterations. As a result, the estimated AUV position drifts, leading to an increasing localization error.

This becomes evident when the AUV moves outside the anchor triangle: the particle cloud expands and develops an elongated or banana-shaped structure, reflecting the increased uncertainty resulting from poor geometric conditioning. This effect of poor particle distribution is illustrated in Figure 5.14.

The particle cloud corresponding to the unfavourable geometry is significantly larger and non-spherical, in comparison to a compact, nearly circular cloud, which reflects the uncertainty, when the AUV remains within the ASV triangle (Figure A.2 appendix A). In regions of unfavourable geometry, incorrectly weighted particles can dominate the posterior PDF and produce biased estimates, which lead to a deviation from the PCRLB.

The deviation from the theoretical achievable RMSE shows, that the EKF and PF

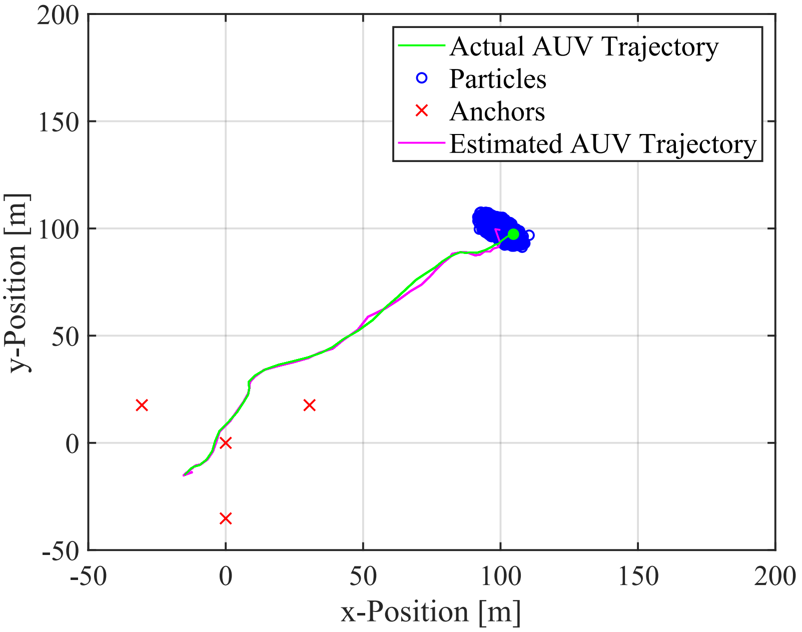

Figure 5.14.: Visualization of particle cloud for poor geometric conditions.

are not optimal filters under such a disadvantageous geometry. These results furthermore underline the importance of maintaining a well-conditioned geometry for trajectory tracking, which can be achieved with appropriate control inputs of the AUV and, when applicable, through coordinated control of the ASVs.

5.3. Design Considerations for Underwater Localization Algorithms

Based on the findings from the simulations, several key considerations can be derived for the design of underwater tracking algorithms.

The tracking should be initialized using a MAP-based estimate of the position and sound speed, where the prior information reflects general environmental conditions that influence the sound speed such as seasonal temperature or salinity.

Both the EKF and the PF represent suitable approaches for trajectory tracking, with the choice depending on the specific localization scenario, for example available computational power and fidelity of the transition model. The simulation results further emphasize the importance of maintaining favorable geometry throughout the tracking process and especially for the initial estimate. The AUV should remain within or close to the area enclosed by the ASVs, as large horizontal spacing can degrade geometric observability and introduce model mismatch in the range estimation. Furthermore, too large horizontal distances combined with rather shallow positions of the AUV can result in a loss of the direct path of acoustic connectivity, as the curvature of the sound rays inherently limits horizontal LoS transmission.

In the next chapter, these findings are applied to acoustic measurement data, collected in the Baltic Sea.

6. Measurement Campaign

In June 2025, the DLR conducted a measurement campaign in the Baltic Sea, off the coast near Gothenburg, Sweden. The campaign aimed at demonstrating the feasibility of using acoustic ranging data to estimate the relative position between the AUV and the ASVs. To this end, the previously investigated localization algorithms were tested using the gathered measurement data.

6.1. Measurement Setup

The measurement campaign was carried out over the course of one week. Five waterproof tubes, each approximately 80 cm long and equipped with hydrophones operating at a frequency of 40 kHz, were used to represent the AUV and ASVs for the acoustic ranging measurements. Four of these tubes served as ASVs, with GPS receivers mounted on one end and hydrophones on the other end. Cylindrical flotation devices ensured that the tubes remained vertically oriented in the water, positioning the hydrophones about 40 cm below, and the GPS receivers approximately 40 cm above the surface. An illustration of these tubes is given in Figure 6.1. The fifth tube, which did not contain a GPS receiver, was equipped with two hydrophones attached to opposite ends of the tube and represents the AUV.

Unlike previous investigations, the ASVs in these experiments were not stationary. However, since their position can be determined via GPS signals, relative position estimation between the ASVs and the AUV is possible.

Because the tubes were not supplied with a propulsion system, different methods were employed to maneuver them during the measurements. The ASVs were connected by a rope, spaced about 7 m apart and towed by a boat, while the AUV was maneuvered using different techniques depending on the experimental setup.

The following paragraphs provide an overview of these configurations for June 13, 14, 17, and 19.

Figure 6.1.: Tubes with hydrophones and GPS receivers that served as ASVs.

June 13 On the 13th of June, the AUV was suspended from a free-floating buoy by two 1.9 m long ropes attached symmetrically on both sides of the tube. A weight was mounted beneath the AUV to keep it aligned with the buoy in the horizontal plane. Therefore the AUV was positioned approximately 1.86 m below the buoy and therefore the surface.

June 14 The following day, the AUV was attached to a second, remotely controlled, boat via a rigid mast, ensuring that the AUV remained fixed approximately 1.5 m underneath the surface. Only one ASV was employed this day.

June 17 and June 19 On the 17th and 19th of June, the AUV was attached on top of a crawler provided by GEOMAR. The crawler was remotely operated and capable of moving along the bottom of the sea at a depth of approximately 10 m in this coastal region.

6.2. Analysis of Ranging Measurements

This section evaluates the ranging measurements with respect to the feasibility of the underlying measurement concept. As demonstrated in Chapter 5, optimized geometry is crucial for the joint estimation of sound speed and positions. In this setup, where the ASVs were towed in one line, the geometry was disadvantageous for this joint estimation and would inevitably lead to a bias in the sound speed estimation. Therefore, the ranges were calculated assuming an average sound speed of 1500 m/s.

The ranging measurements recorded on June 13, obtained from two experiments conducted with the configuration described above, are illustrated in Figure 6.2. The results from the other days are provided in Appendix A.

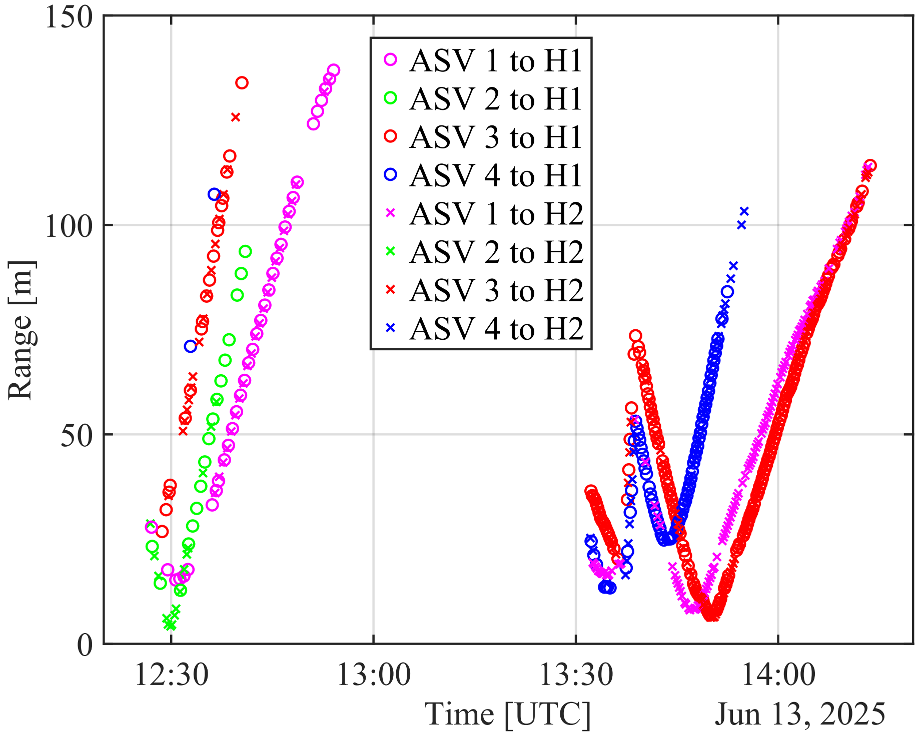

Figure 6.2.: Range measurements obtained on the 13th of June, calculated with an average sound speed of 1500 m/s.

ASV1 to ASV4 correspond to the hydrophones mounted on the different ASVs, while H1 and H2 represent the hydrophones, on opposite sides of the AUV. While most hydrophones provide consistent measurements only limited data is available from ASV 4 during the first experiment, and none from ASV 2 during the second. The ranges measured between the ASVs and the AUV demonstrate consistent trends, which can be attributed to the ASVs being towed in one line by a single boat. The continuous rise and fall of the ranging measurements reflect the boat's movement: As the boat moved farther away from the AUV, all the ranges increased at the same rate and vice versa. This confirms that the calculated ranges are consistent and reliable.

Region Without Line of Sight Connection

A comparison of the range estimates from the various measurements reveals that at a certain point, the communication between the vehicles breaks off. The threshold for this connection loss increases with the depth of the receiving hydrophone, which confirms that the loss of LoS connection is depth-dependent.

This behaviour for the different range estimates is illustrated in Figure 6.3. The receiver depth of 0.4 m corresponds to ranges that were measured between two different ASVs, the receiver depth of 1.5 m to ranges measured between the ASVs and AUV on June 14, 1.86 m to June 13 and the depth of 10 m to the 17th and 19th of June. The black curve represents the theoretical threshold for a LoS connection, calculated using the model presented in Section 3.3.3, with an approximation of the sound speed gradient corresponding to the SSP in Figure 2.4(a) and an initial sound speed c_0 of 1500 m/s.

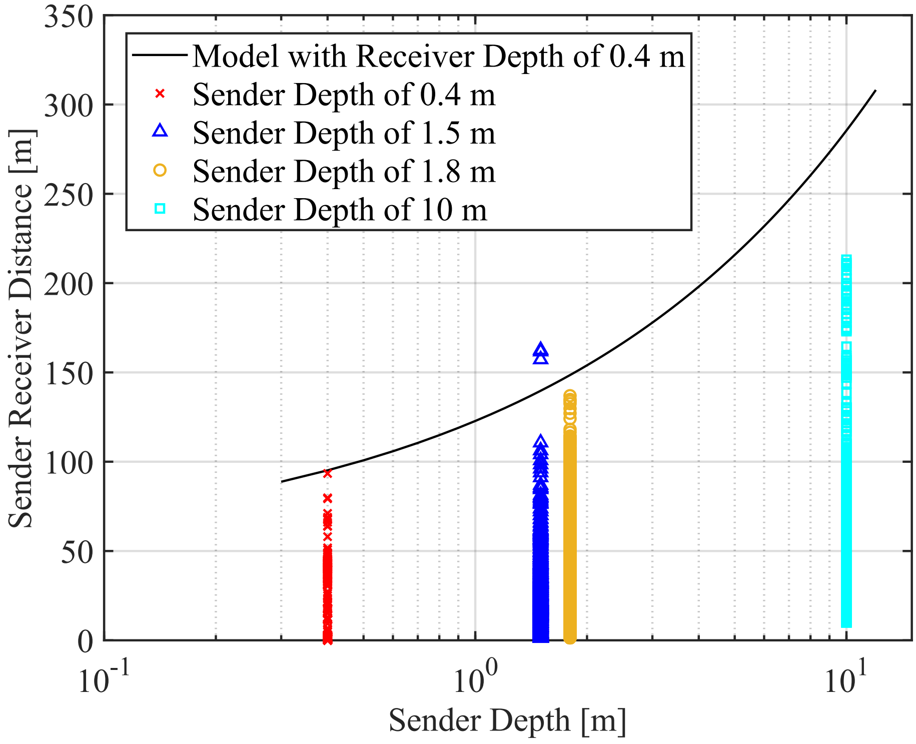

Figure 6.3.: Comparison of measured and modeled ranges illustrating the LoS distance as a function of sender depth, for a receiver depth of 0.4 m.

It can be observed that the measured ranges approximate the theoretical curve. The outliers for the sender depth of 1.5 m can be attributed to stochastic effects, that can increase the LoS communication region, such as surface waves that effectively increase the sender- and receiver depth, thereby extending the LoS connectivity region for that time. The circumstance that the depth-dependent maximum ranges converge towards the modeled curve validates the applicability of this model - with appropriate approximations about the SSP - for acoustic ranging applications in shallow waters.

Multipath Propagation

The ranging measurements illustrated in Figure 6.2, exhibit a clear absence of significant outliers. This indicates that at the operating frequency of the hydrophones, direct and reflected rays - with greater time delays than 25 µs - can be distinguished. Consequently, the hypothesis stated in Chapter 3, that multipath propagation does not compromise the localization performance for this configuration, is confirmed.
The hydrophones distinguish between LoS propagation and NLoS propagation based on the arrival times of the signal. Figure 6.2 and Figure 6.3 further reveal that as soon as the LoS signal is lost, there is a total absence of ranging signals, meaning that in this region likewise, the vehicles do not mistakenly identify a reflected ray as LoS. The is due to the fact that for distances exceeding the maximum LoS connectivity region, practically only rays that have been reflected at least once on the bottom of the ocean, or other obstacles, can reach the AUV. These reflected rays experience such a significant energy loss - likely due to absorption by the seabed - that they are not detected by the hydrophones and therefore not included in the measurements.
The fact that rays which are only reflected at the surface cannot reach the NLoS connectivity region can be visualized with the simplified model, in which every acoustic ray gets bent on a curve with the radius R. This radius is determined based on the gradient of the SSP as well as the initial angle of the ray γ_0

$$R = -\frac{c_0}{-g\cos\gamma_0}.$$

The maximum LoS distance corresponds to the maximum initial angle γ_0 for which the ray does not get reflected at the surface of the ocean. The relationship between R and γ_0 reveals that the radius of the ray curvature, increases with larger initial angle γ_0 (horizontal launch: $\gamma_0 = 0°$). As the initial angle γ_0 becomes too large for LoS connection, the ray intersects the sea surface closer to the transmitter, marking the highest point of its trajectory. At this point, the ray is reflected downward with equal angles of incidence and reflection, continuing along a curved path determined by the exit angle.

The maximum LoS ray reaches the surface without reflection, thus its highest point of trajectory extends farthest horizontally.

For a constant sound speed gradient and relatively small transmitter and receiver depths, the total horizontal range of rays reflected at the surface remains shorter than that of the maximum LoS ray. Although the reflected ray follows a path with a larger curvature radius, the reflection angle causes the ray to propagate downward rather than horizontally, therefore the additional path after reflection can not compensate for the shorter distance covered before reflection.

This behaviour is illustrated in Figure 6.4 for a sender depth of 0.4 m and a receiver depth of 1.5 m. Analogous to the ray-figures in Chapter 2 and 3 the red rays represent LoS paths, while the green rays correspond to a single reflection at the surface. It has to be noted, that this is idealized behaviour, based not only on linearly changing sound speed, but also an even surface of the ocean.

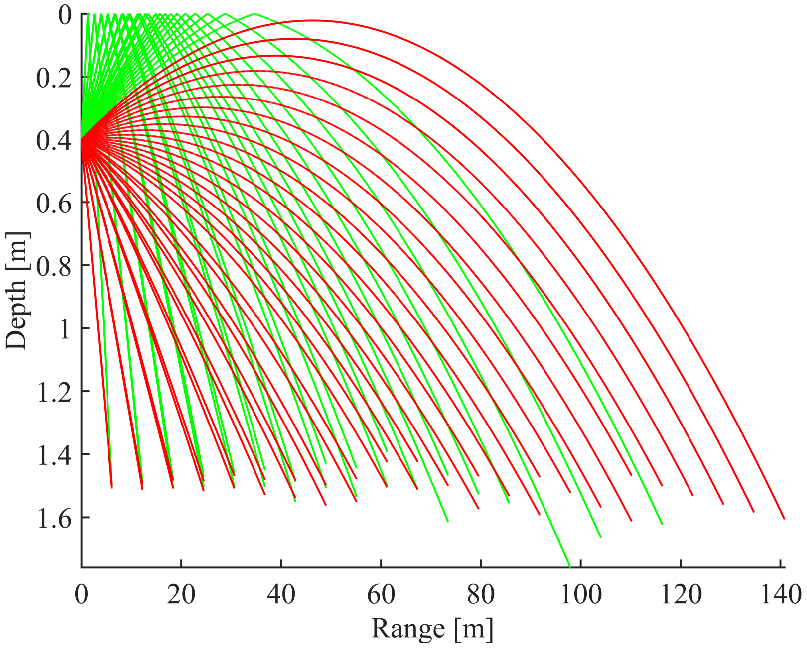

Figure 6.4.: Farthest ray propagation for a sender depth of 0.4 m and a receiver depth of 1.5 m

6.3. Localization Based on Experimental Data

The ranging data from June 17, illustrated in Figure 6.5, was selected for an exemplary localization algorithm, as this day presents the most promising results with regard to both range and GPS measurements.

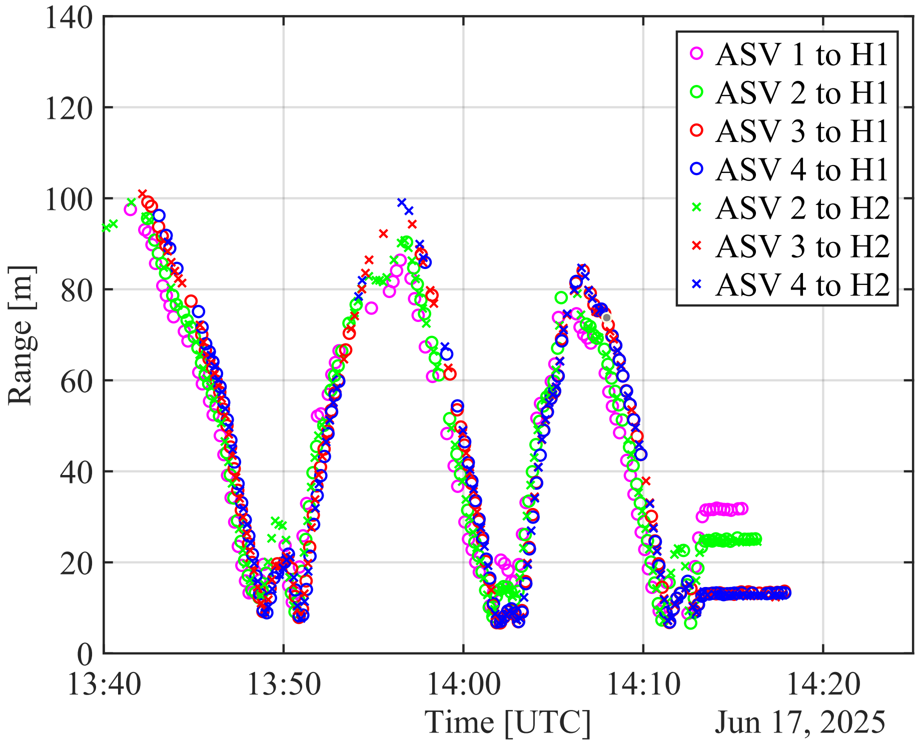

Figure 6.5.: Range measurements obtained on the 17th of June, calculated with an average sound speed of 1500 m/s.

A PF was implemented for the localization estimates due to its flexibility and its capability to visualize estimation uncertainty via the corresponding particle cloud. Owing to the unfavourable geometry, no joint estimation of position and sound speed was performed and the PF was initialized with a ML position estimate derived from the ranges calculated based on a sound speed of 1500 m/s.

The transition model was defined without explicit control inputs that reflect deterministic relative movement between the AUV and ASVs, as there is no information available about the planned relative movement between the vehicles. To compensate for this lack of information, the noise of the transition model was increased. Figure 6.6(a)-(d) was selected to illustrate the performance of the PF at different time steps. The first and the last time steps correspond to the earliest and the latest available range measurements, the intermediate time steps represent different stages of the PFs development.

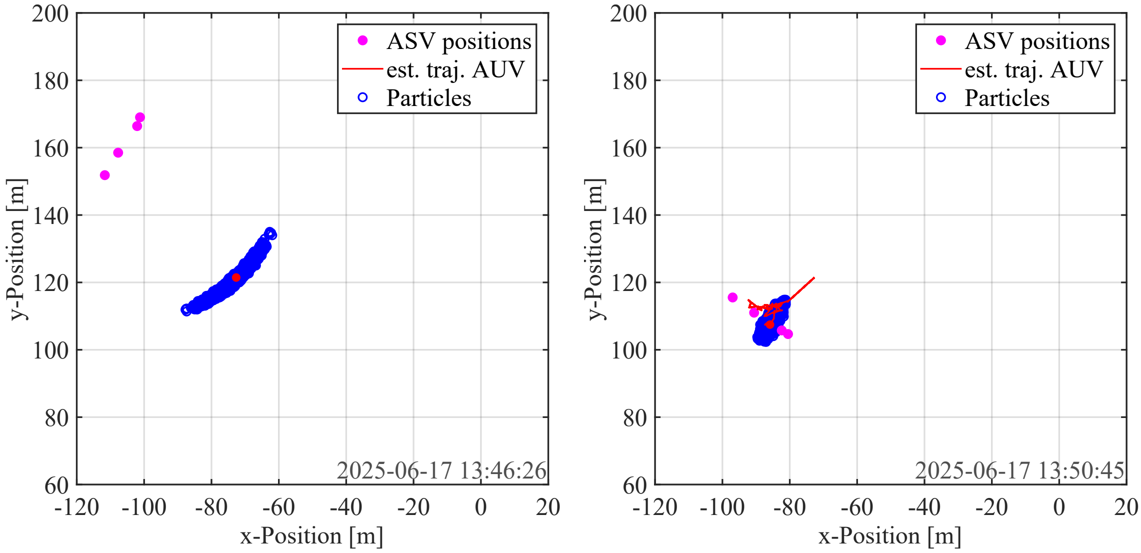

(a) At the first time step (b) After 4 minutes (favourable geometry)

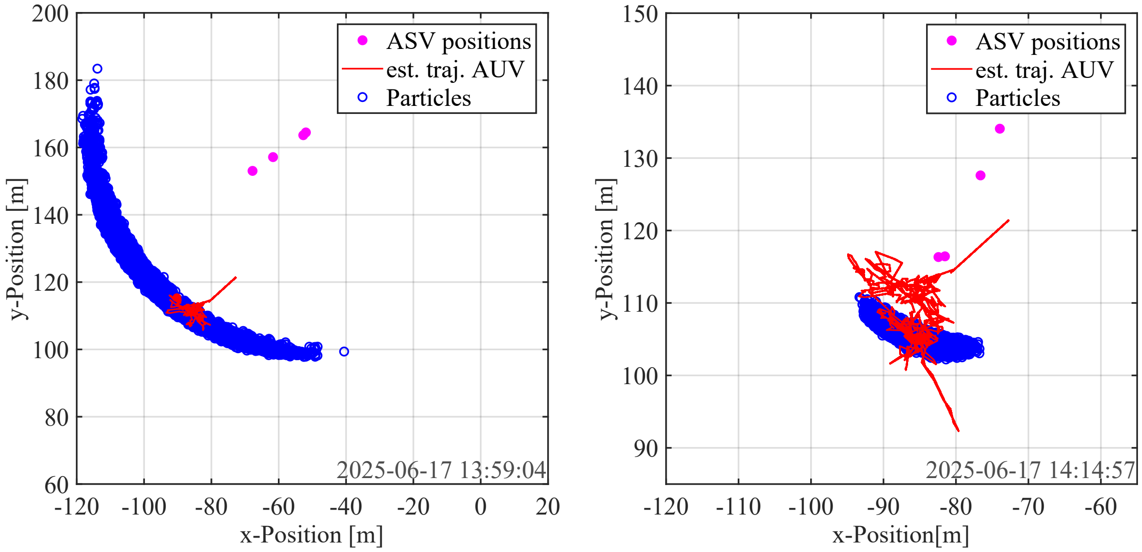

(c) After 14 minutes (poor geometry). (d) At the last time step

Figure 6.6.: PF on July 17 at (a) the first time step, (b) after four minutes, (c) after 14 minutes, and (d) at the last time step.

It can be observed, that localization with that setup is feasible and enables continuous tracking of the relative motion between the AUV and the ASVs. Although no ground truth data is available to quantify the performance of the position estimation and evaluate possible influence of a bias caused by wrongly assumed sound speed or poor geometry, several qualitative aspect can be identified. The estimated position of the AUV changes only gradually over time, while the ASVs exhibit faster movement. This behaviour is consistent faster motion of the towing boat and the limited mobility of the underwater crawler, to which the AUV was attached.

The performance of the PF for different geometric conditions is further illustrated in Figure 6.6(b) and Figure 6.6(c). The particle cloud for a filter configuration with rather favourable geometric conditioning is depicted in Figure 6.6(b), where the ASVs are in close proximity to the estimated position of the AUV, such that two main directional gradient can be identified - one approximately along the towing direction of the boat and one perpendicular to it. The ranging measurements from these directions provide complementary information, which improve the localization accuracy and results in an elliptically shaped particle cloud. The longer axis of the ellipse corresponds to the direction in which no range information is available.

In contrast, the geometry illustrated in Figure 6.6(c) is unfavourable, as the ASVs are aligned almost in one line with the AUV. Consequently, their directional gradients are nearly identical, leading to a banana shaped particle cloud which represents the increased estimation uncertainty. This configuration can cause biased particles to receive disproportionately high weights, resulting in biased position estimates.

The observed behaviour underlines the importance of optimized geometric conditioning discussed in Section 5.2.1.

7. Conclusion

This thesis presents a comprehensive investigation into the challenges associated with short range underwater localization, with a focus on the interrelations between geometric configuration, sound speed estimation, and filter initialization.

A central problem with ASV based localization is that the ASVs are constrained to a common horizontal plane, leading to localization difficulties for non-optimized geometric conditioning within this constraint. It is demonstrated that tracking algorithms based on the EKF and PF, when initializing with Maximum A-Posteriori estimation, show highly promising performance. This initialization strategy allows for accurate joint estimation of sound speed and position, while mitigating the risk of large initial estimation bias due to poor geometry, by incorporating prior knowledge about the sound speed. The accuracy of this prior knowledge is greatly improved by rough estimation of environmental parameters like seasonal temperature or salinity. The estimation results confirm that joint estimation of position and sound speed, particularly during initialization phases, enhance the robustness of the algorithm against erroneous prior assumptions by preventing the propagation of persistent biases that otherwise degrade range estimates. A key insight from the analysis is that unfavourable initial geometry not only reduces precision, but can also induce long-lasting bias in the sound speed estimation, which propagates systematically into range estimations. This underlines the importance of geometric conditioning for practical deployment scenarios.

The impact of model mismatch caused by depth-dependent sound speed variations, which result in refraction and different average sound velocities along the individual propagation paths, is evaluated as well. For short range applications those sound speed variations result in negligible deviations when assuming a constant average sound speed for different propagation paths, provided that the spatial separation between the AUV and ASVs remains comparable. This validates the use of a simplified propagation model, allowing for ranging based on an effective average sound speed and an Euclidean distance between the different vehicles.

However, the simulations have revealed that as range disparities increase, the average sound speed for the different propagation paths deviate more strongly from one another, implying that for the simplified measurement model, limitations for horizontal spacing must be applied. Moreover, due to ray refraction, horizontal LoS propagation is inherently limited, further constraining the inter-vehicle ranges in horizontal direction.

Data collected during a dedicated measurement campaign demonstrates that consistent position estimation is achievable for this setup under real underwater conditions. The measurement data confirmed the limitations of the estimation performance for unfavourable geometric conditioning. Furthermore, the restrictions on inter-vehicle LoS connectivity at large horizontal spacing were evident in the data, validating the practical relevance of this limit. In addition, the derived model for the maximum LoS distance in shallow waters accurately approximates the depth-dependent communication range. An integration of this model into swarm control and swarm navigation algorithms allow for continuous evaluation of the LoS condition and therefore ensures connectivity and mission reliability.

In conclusion, this thesis establishes that successful short range underwater localization not only depends on filtering techniques but on a holistic consideration of geometry, initialization and environmental modeling, with special constraints regarding maximum LoS connectivity for swarm control applications.

8. Outlook

The next step in advancing an underwater localization system is to expand the setup to cover a wider area. This can be achieved by employing more ASVs and AUVs to create a network encompassing a larger region, and by increasing spacing between the ASVs and AUV. The latter would be possible in terms of signal transmission properties, due to the low attenuation of acoustic signals underwater. This enables communication over large distances, although it is limited by the LoS constraint imposed by the curvature of the acoustic rays.

To maintain localization accuracy in a more widely spaced setup, different approaches could be considered. One possibility would be to incorporate barometric measurements to estimate the depth (z-position) of the AUV. This would reduce the ambiguity in coupled sound speed and position estimation, effectively reducing the estimation uncertainty.

Another potential improvement would be to incorporate a range- and depth-dependent correction term. Due to the depth-dependent variations in the sound speed, different ray paths effectively experience different average sound speeds. Generally, the sound speed experienced by rays that travel larger horizontal distances, is higher than that experienced by rays that travel mainly vertically. If the average sound speed for a specific propagation path - for example direct vertical propagation - is known, this correction term could account for these variations, by determining a higher sound speed for rays that travel larger horizontal distances. With such a setup, an initial accurate estimation of the sound speed would still be crucial, as this initial estimation would serve as the reference on which the correction factor would be imposed to account for path-specific variations.

An additional way to increase accuracy could be to eliminate the need for estimation of both sound speed and position, as this joint approach leads to biased estimation in poor geometric conditions. This could be achieved by including temperature sensors in the ASVs and AUV. Roughly assuming the salinity of the given body of water - for example, the Baltic sea has very low salinity, whereas oceans usually exhibits higher salinity - and utilizing the temperature measurements from the ASVs and the AUV enables the calculation of the sound speed at those depth with the Medwin model. Furthermore, assuming a linear gradient of the sound speed profile for the given water mass would allow for an approximation of the sound speed profile within that region. This knowledge could further improve the correction term for the path-specific variations in the average sound speed, as it does not only incorporate tendencies - higher sound speed for larger horizontal ranges -, but the actual approximated sound speed profile.

These approaches could initially be tested via simulations using Bellhop to capture the differences between the approximated ray specific average sound speed and the more realistically simulated sound speed. Subsequently, they could be validated with a measurement campaign, for instance by fixing the AUV to a stationary underwater crawler. This setup would allow for precise ground truth acquisition - using the crawlers initial position for horizontal reference and barometer measurements for depth - while the GPS-equipped ASVs are moved to asses relative positioning performance.

Bibliography

[1] "Gas leaks from Nord Stream 1 & 2." [Online]. Available: https://www.io-warnemuende.de/short-news-archive-details/items/gas-leaks-from-nord-stream-1-2.html

[2] "Titan Submersible - Coast Guard Marine Board of Investigation." [Online]. Available: https://www.news.uscg.mil/News-by-Region/Headquarters/Titan-Submersible/

[3] "Gelände und Unterwasser-Topographie - Fraunhofer IPM." [Online]. Available: https://www.ipm.fraunhofer.de/de/gf/objekterfassung-laserscanning/anw/unterwasser-laserscanning/unterwasser-topographie-bathymetrie.html

[4] "World's most accurate positioning service, Galileo's HAS, goes live - European Commission," Dec. 2024. [Online]. Available: https://joint-research-centre.ec.europa.eu/jrc-news-and-updates/worlds-most-accurate-positioning-service-galileos-has-goes-live-2023-01-24_en

[5] U. M. Qureshi, F. K. Shaikh, Z. Aziz, S. M. Z. S. Shah, A. A. Sheikh, E. Felemban, and S. B. Qaisar, "RF Path and Absorption Loss Estimation for Underwater Wireless Sensor Networks in Different Water Environments," *Sensors (Basel, Switzerland)*, vol. 16, no. 6, p. 890, Jun. 2016. [Online]. Available: https://www.ncbi.nlm.nih.gov/pmc/articles/PMC4934316/

[6] X. Su, I. Ullah, X. Liu, and D. Choi, "A Review of Underwater Localization Techniques, Algorithms, and Challenges," *Journal of Sensors*, vol. 2020, no. 1, p. 6403161, 2020, _eprint: https://onlinelibrary.wiley.com/doi/pdf/10.1155/2020/6403161. [Online]. Available: https://onlinelibrary.wiley.com/doi/abs/10.1155/2020/6403161

[7] Q. Wang, H.-N. Dai, X. Li, H. Wang, and H. Xiao, "On Modeling Eavesdropping Attacks in Underwater Acoustic Sensor Networks," *Sensors*,

vol. 16, no. 5, p. 721, May 2016. [Online]. Available: https://www.mdpi.com/1424-8220/16/5/721

[8] S. Badri-Höher, “Underwater Techniques,” *University of Applied Sciences Kiel, Faculty of Computer Science and Electrical Engineering, Summerterm 2017*, 2017.

[9] M. Stojanovic, “On the relationship between capacity and distance in an underwater acoustic communication channel,” *ACM SIGMOBILE Mobile Computing and Communications Review*, vol. 11, no. 4, pp. 34–43, Oct. 2007. [Online]. Available: https://dl.acm.org/doi/10.1145/1347364.1347373

[10] M. Stojanovic and J. Preisig, “Underwater acoustic communication channels: Propagation models and statistical characterization,” *IEEE Communications Magazine*, vol. 47, no. 1, pp. 84–89, Jan. 2009. [Online]. Available: https://ieeexplore.ieee.org/document/4752682/

[11] L. M. Brechovskich and Y. P. Lysanov, *Fundamentals of Ocean Acoustics*, 3rd ed., ser. Modern Acoustics and Signal Processing. New York, NY: Imprint: Springer, 2003.

[12] “Baltic Thalweg - IOW.” [Online]. Available: https://www.io-warnemuende.de/baltic-thalweg-transect.html

[13] J.-j. Wang, T. Lin, and J. Fu, “Analysis of Effective Sound Velocity Spatial Characteristic of Typical MUNK Deep Sea Channel,” in *2018 IEEE 8th International Conference on Underwater System Technology: Theory and Applications (USYS)*, Dec. 2018, pp. 1–6. [Online]. Available: https://ieeexplore.ieee.org/document/8778987/

[14] J. M., “Ray Trace Modeling of Underwater Sound Propagation,” in *Modeling and Measurement Methods for Acoustic Waves and for Acoustic Microdevices*, M. G. Beghi, Ed. InTech, Aug. 2013. [Online]. Available: http://www.intechopen.com/books/modeling-and-measurement-methods-for-acoustic-waves-and-for-acoustic-microdevices/ray-trace-modeling-of-underwater-sound-propagation

[15] M. B. Porter and the Regents of the University of California, “Bellhop: Underwater acoustics simulator,” 2023, accessed: 2025-5-06. [Online]. Available: https://github.com/A-New-BellHope/bellhop/tree/main/Bellhop

[16] S. Kale, “Developments in Unmanned Surface Vehicles (USVs): A Review,” *International Conference on Applied Engineering and Natural Sciences*, vol. 1, no. 1, pp. 596–600, Jul. 2023. [Online]. Available: https://as-proceeding.com/index.php/icaens/article/view/1064

[17] S. M. Kay, *Fundamentals of statistical signal processing: estimation theory*. USA: Prentice-Hall, Inc., 1993.

[18] P. Tichavsky, C. Muravchik, and A. Nehorai, “Posterior Cramer-Rao bounds for discrete-time nonlinear filtering,” *IEEE Transactions on Signal Processing*, vol. 46, no. 5, pp. 1386–1396, May 1998. [Online]. Available: http://ieeexplore.ieee.org/document/668800/

[19] “Cramér Rao Lower Bound - Navipedia.” [Online]. Available: https://gssc.esa.int/navipedia/index.php/Cram%C3%A9r_Rao_Lower_Bound

[20] S. Zhang, R. Raulefs, A. Dammann, and S. Sand, “System-level performance analysis for Bayesian cooperative positioning: From global to local,” in *International Conference on Indoor Positioning and Indoor Navigation*, Oct. 2013, pp. 1–10. [Online]. Available: https://ieeexplore.ieee.org/document/6817888/

[21] M. Z. Win, Y. Shen, and W. Dai, “A Theoretical Foundation of Network Localization and Navigation,” *Proceedings of the IEEE*, vol. 106, no. 7, pp. 1136–1165, Jul. 2018. [Online]. Available: https://ieeexplore.ieee.org/document/8421288/

[22] W. Rudin, *Real and complex analysis*, 3rd ed., ser. McGraw-Hill international editions Mathematics series. New York, NY: McGraw-Hill, 2013.

[23] R. A. Willoughby, “Solutions of Ill-Posed Problems (A. N. Tikhonov and V. Y. Arsenin),” *SIAM Review*, vol. 21, no. 2, pp. 266–267, 1979, _eprint: https://doi.org/10.1137/1021044. [Online]. Available: https://doi.org/10.1137/1021044

[24] “fmincon - Find minimum of constrained nonlinear multivariable function - MATLAB.” [Online]. Available: https://de.mathworks.com/help/optim/ug/fmincon.html

[25] J. S and M. Bakar, “An analysis on sound speed in seawater using ctd data,” *Journal of Applied Sciences*, vol. 10, 02 2010.

[26] A. Doucet, N. d. Freitas, and N. J. Gordon, Eds., *Sequential Monte Carlo Methods in Practice*, ser. Statistics for Engineering and Information Science. Springer, 2001.

[27] S. Särkkä, *Bayesian Filtering and Smoothing*, ser. Institute of Mathematical Statistics Textbooks. Cambridge: Cambridge University Press, 2013. [Online]. Available: https://www.cambridge.org/core/product/C372FB31C5D9A100F8476C1B23721A67

[28] J. Nocedal and S. J. Wright, *Numerical optimization*, 2nd ed., ser. Springer series in operations research and financial engineering. New York, NY: Springer, 2006.

A. Additional Figures

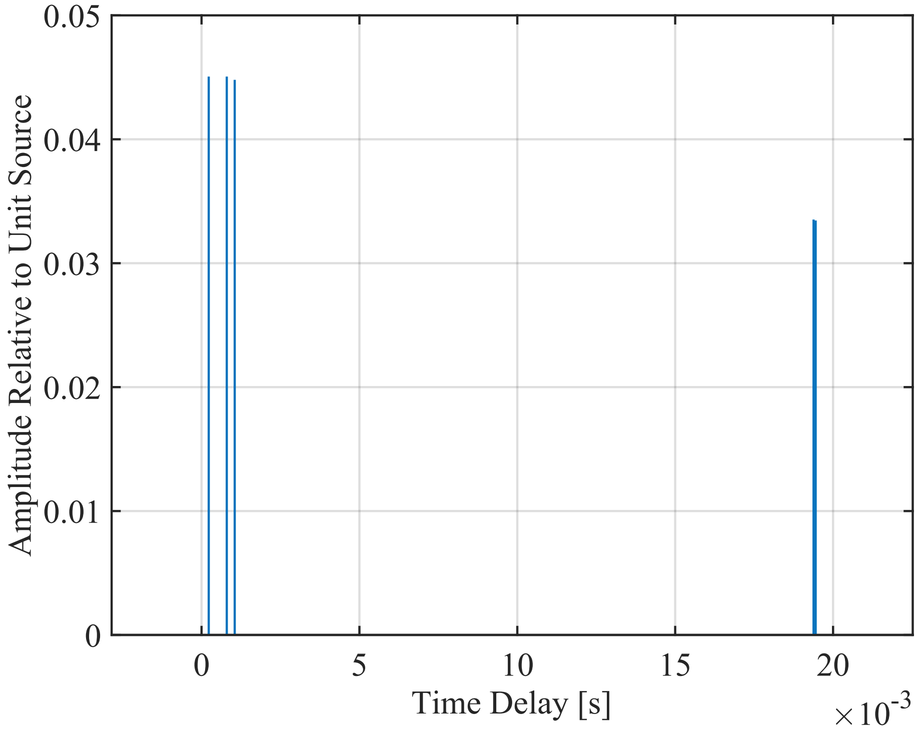

Figure A.1.: Impulse response at the receiver for a 50 m horizontal range.

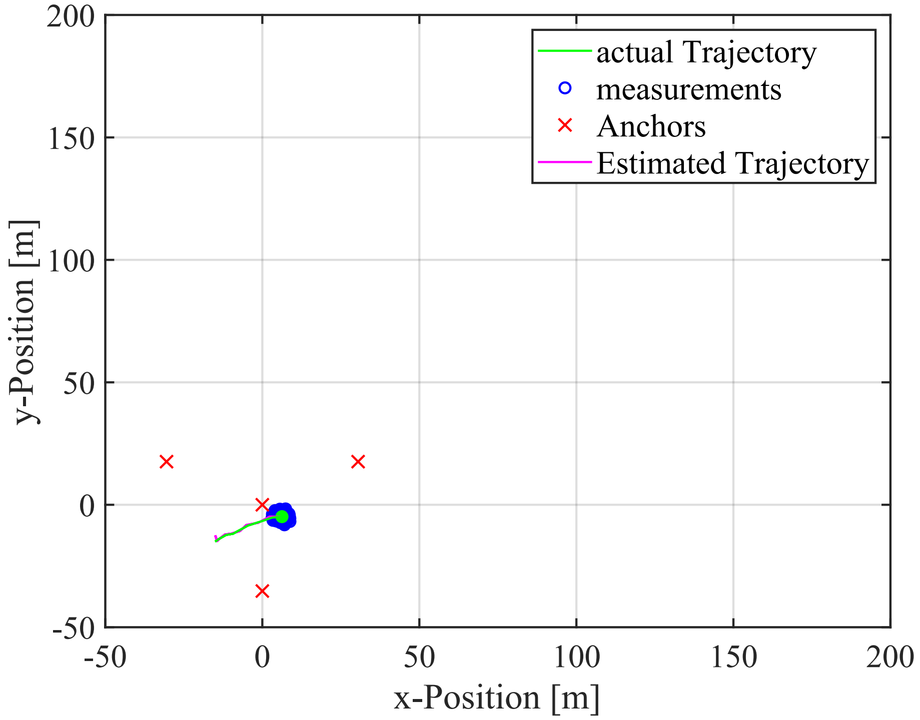

Figure A.2.: Particle cloud for favourable geometric conditions.

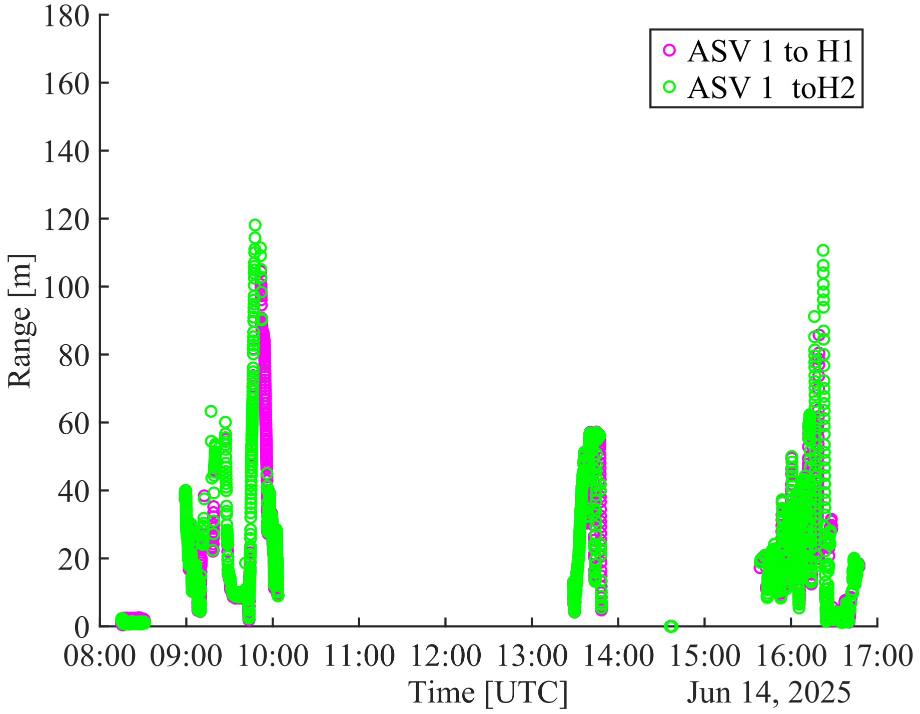

Figure A.3.: Range measurements obtained on the 14th of June, calculated with an average sound speed of 1500 m/s.

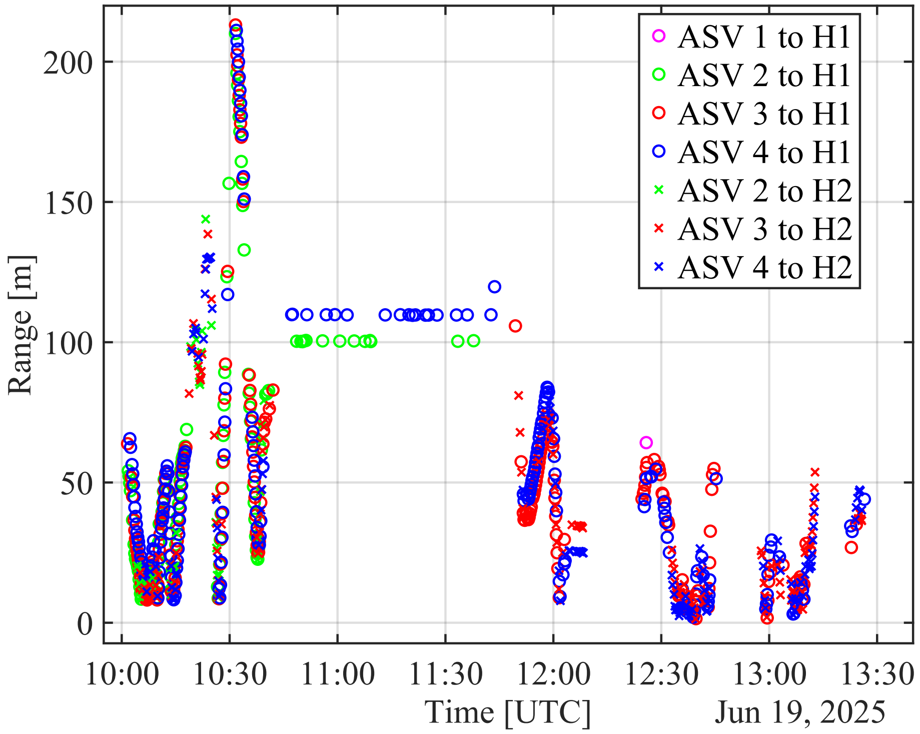

Figure A.4.: Range measurements obtained on the 19th of June, calculated with an average sound speed of 1500 m/s.